

**DESIGN AND TESTING OF PIEZOELECTRIC SENSORS**

A Thesis

by

**BARTOSZ MIKA**

Submitted to the Office of Graduate Studies of  
Texas A&M University  
in partial fulfillment of the requirements for the degree of

**MASTER OF SCIENCE**

August 2007

Major Subject: Mechanical Engineering

# DESIGN AND TESTING OF PIEZOELECTRIC SENSORS

A Thesis

by

BARTOSZ MIKA

Submitted to the Office of Graduate Studies of  
Texas A&M University  
in partial fulfillment of the requirements for the degree of

MASTER OF SCIENCE

Approved by:

Chair of Committee,  
Committee Members,

Department Head,

Hong Liang  
Won-jong Kim  
Sunil Khatri  
Dennis O'Neal

August 2007

Major Subject: Mechanical Engineering

**ABSTRACT**

Design and Testing of Piezoelectric Sensors. (August 2007)

Bartosz Mika, B.S., University of Washington

Chair of Advisory Committee: Dr. Hong Liang

Piezoelectric materials have been widely used in applications such as transducers, acoustic components, as well as motion and pressure sensors. Because of the material's biocompatibility and flexibility, its applications in biomedical and biological systems have been of great scientific and engineering interest. In order to develop piezoelectric sensors that are small and functional, understanding of the material behavior is crucial. The major objective of this research is to develop a test system to evaluate the performance of a sensor made from polyvinylidene fluoride and its uses for studying insect locomotion and behaviors. A linear stage laboratory setup was designed and built to study the piezoelectric properties of a sensor during buckling deformation. The resulting signal was compared with the data obtained from sensors attached a cockroach, *Blaberus discoidalis*. Comparisons show that the buckling generated in laboratory settings can be used to mimic sensor deformations when attached to an insect. An analytical model was also developed to further analyze the test results. Initial analysis shows its potential usefulness in predicting the sensor charge output. Additional material surface characterization studies revealed relationships between microstructure properties and the piezoelectric response. This project shows feasibility of studying insects with the use of polyvinylidene fluoride sensors. The application of engineering materials to insect

studies opens the door to innovative approaches to integrating biological, mechanical and electrical systems.

## ACKNOWLEDGEMENTS

I would like to express my gratitude to Dr. Hong Liang for her support and guidance during the course of this project, and to Dr. Jingang Yi for his assistance, especially with the early system design and mathematical analysis.

Additional thanks go to the members of my graduation committee, Dr. Sunil Khatri and Dr. Won-jong Kim, for their assistance with the thesis and its defense, as well as Dr. Jorge Gonzalez for his help with insect testing. Thanks to Hyungoo Lee for assistance with AFM studies, and to all members of the research team for their suggestions and constructive discussions throughout my involvement with the project.

I would also like to thank my parents who have provided continuous encouragement to all my educational pursuits. They always been there to help me through the challenges along the way. I certainly wouldn't have made it this far without them.

Finally, I would like to acknowledge the National Science Foundation for their financial support of this project (grant number IIS-0515930).

## TABLE OF CONTENTS

	Page
ABSTRACT .....	iii
ACKNOWLEDGEMENTS .....	v
TABLE OF CONTENTS .....	vi
LIST OF FIGURES ... ..	viii
LIST OF TABLES .....	x
NOMENCLATURE .. ..	xi
CHAPTER I INTRODUCTION.....	1
I.1 History of piezoelectricity .....	2
I.2 Introduction to the polyvinylidene fluoride (PVDF) .....	2
I.3 Piezoelectric behavior overview .....	7
I.4 Piezoelectric mechanism research .....	9
I.5 General piezoelectric equations .....	10
I.6 Linear piezoelectricity .....	14
I.7 Manufacturing processes .....	18
I.8 Applications .....	21
I.9 Motivation and objectives .....	22
I.10 Approaches .....	24
CHAPTER II SENSOR FABRICATION .....	26
II.1 Materials .....	26
II.2 Material properties .....	26
II.3 Sensor synthesis .....	28
II.3.1 Metallization .....	28
II.3.2 Sensor preparation .....	29
II.3.3 Lead attachment methods .....	29
II.4 Sensor mounting .....	31
CHAPTER III EXPERIMENTAL SETUP .....	34
III.1 Sensor testing background .....	34
III.2 Insect testing setup .....	36

	Page
III.3 Laboratory setup .....	37
III.3.1 Mechanical setup .....	38
III.3.2 Deflection distance gauge .....	39
III.4 System control and data acquisition setup .....	42
III.4.1 Motion control .....	44
III.4.2 Position feedback .....	44
III.4.3 Sensor signal output .....	44
III.4.4 Data transfer and analysis .....	46
III.5 Atomic force microscopy studies .....	46
 CHAPTER IV RESULTS AND ANALYSIS .....	 49
IV.1 Laboratory measurements .....	49
IV.2 Roach experiments .....	52
IV.3 Analytical modeling .....	54
IV.3.1 Stress considerations .....	54
IV.3.2 Existing buckling models .....	54
IV.3.3 Analytical models .....	55
IV.3.4 Lateral deflection analysis .....	56
IV.3.5 Model comparisons .....	56
IV.4 Microscopic analysis results .....	58
 CHAPTER V CONCLUSIONS .....	 63
 REFERENCES .....	 65
 APPENDIX A EQUATIONS AND DERIVATIONS .....	 70
 APPENDIX B LABORATORY EQUIPMENT SETUP .....	 78
 VITA .....	 97

## LIST OF FIGURES

	Page
Figure 1 Polyvinylidene fluoride molecule.....	3
Figure 2 Diagrams of (a) $\alpha$ -phase and (b) $\beta$ -phase chain conformations in PVDF. ....	4
Figure 3 Polarizing microscope image of PVDF spherulites.....	5
Figure 4 PVDF spherulite structure diagram. ....	6
Figure 5 Diagram of a PVDF lamellar crystal and its dipole orientation. ....	8
Figure 6 Relationships among material properties. ....	11
Figure 7 Tensor directions for constitutive relation definitions.....	12
Figure 8 PVDF manufacturing process.....	19
Figure 9 Crystal lamellae and amorphous regions within PVDF: (a) melt cast; (b) structure alignment through mechanical stretching; (c) lamellae oriented due to electrical poling.....	20
Figure 10 Discoid roach ( <i>Blaberus discoidalis</i> ) – relative size (L-female, R-male). ....	23
Figure 11 Buckling, stretching and bending deflections. ....	25
Figure 12 Detailed sensor schematic. ....	30
Figure 13 Image of a complete sensor. ....	31
Figure 14 Sensor locations across roach leg joints. ....	32
Figure 15 Scanning electrode microscope (SEM) image of roach leg with a sensor. ....	33
Figure 16 Side-view schematic of sensor mounting and deformations – arrows indicate motion directions.....	35
Figure 17 Roach testing attachment.....	36
Figure 18 Overview of experimental setup.....	37
Figure 19 Sensor mounting setup with the linear stage shown on the right. ....	38
Figure 20 Sensor mounting setup. ....	39



	Page
Figure 21 Laser distance gauge setup; (a) side view, (b) angled top view. ....	40
Figure 22 Sensor lateral deflection measurement. Reference position is shown at the sensor mount. ....	41
Figure 23 Laboratory system diagram. ....	43
Figure 24 Charge amplifier circuit. ....	45
Figure 25 Schematic diagram of AFM operation. ....	47
Figure 26 Pacific Nanotechnology Nano-R™ atomic force microscope. ....	48
Figure 27 Sensor charge output in relationship to buckling deflection. ....	49
Figure 28 Sensor piezoelectric response in relationship to buckling amplitude. ....	50
Figure 29 Sensor piezoelectric response in relationship to buckling frequency. ....	51
Figure 30 Sensor charge generated due to roach movement. ....	52
Figure 31 Average peak charge comparisons for various insect movement speeds. ....	53
Figure 32 Graphs of normalized sensor charge and sensor-end axial displacement $\delta$ during buckling. ....	55
Figure 33 Sensor output in relationship to buckling deflection – laboratory results. ....	57
Figure 34 Sensor output in relationship to buckling deflection – scaled analytical results. ....	57
Figure 35 AFM height and phase images of the PVDF material. ....	59
Figure 36 AFM Line scans with no applied potential: (a) horizontal, (b) vertical. ....	60
Figure 37 Line scans with 5V applied potential: (a) horizontal, (b) vertical. ....	61

**LIST OF TABLES**

	Page
Table 1 Properties of PVDF film. ....	27
Table 2 PVDF sample AFM line scans - surface height comparisons. ....	61

## NOMENCLATURE

PVDF	Poly (Vinylidene Fluoride)
PVF2	Poly (Vinylidene Fluoride)
AFM	Atomic Force Microscope
Å	1 Angstrom (Å) = $10^{-10}$ meter (m)
D	Traditional dipole moment unit – Debye (D) = $3.34 \times 10^{-30}$ C-m
$T_g$	Glass transition temperature
$T_c$	Curie transition temperature
S	Mechanical stress – Pa = N/m <sup>2</sup>
T	Mechanical strain – dimensionless
E	Electric intensity – V/m
D	Electric displacement – C/m
$\epsilon^T, \epsilon^S$	Permittivity – F/m = C/(mV)
$\beta^T, \beta^S$	Impermeability – m/F = (mV)/C
e	Piezo constant – C/m <sup>2</sup> = N/(mV)
d	Piezo constant – m/V = C/N
h	Piezo constant – V/m = N/C
g	Piezo constant – m <sup>2</sup> /C = (mV)/N
$c^E, c^D$	Elastic stiffness – Pa = N/m <sup>2</sup> = J/m <sup>3</sup>
$s^E, s^D$	Compliance – Pa <sup>-1</sup> = m <sup>2</sup> /N = m <sup>3</sup> /J
$\epsilon_0$	Permittivity of vacuum = $8.854 \times 10^{-12}$ (F/m)
$d_{31}$	Transverse piezoelectric constant
$d_{33}$	Longitudinal piezoelectric constant

$dA$	Piezoelectric film electrode area
$q$	Electrical charge in the piezoelectric sensor
$C_p$	Capacitance of the piezoelectric sensor (C)
$C_c$	Capacitance of the sensor wire leads (C)
$C_F$	Charge amplifier feedback loop capacitance (C)
$R_F$	Charge amplifier feedback loop resistance (M $\Omega$ )
$\delta$	Axial deflection during buckling deformation
$L$	Half of sensor length
$h$	Sensor thickness
$I$	Sensor cross-sectional moment of inertia
$Q_e$	Electrical charge approximated at quasi-static conditions

## CHAPTER I

### INTRODUCTION

The last century has been a time of strong growth of the industry and its influence on the world's population. Today, innovation and technology lead people into areas once never imagined. Miniaturization, remote control, rapid information transfer, or biomedical implants for improved healing are only a few examples. None of these would be possible without advanced materials such as polymers. Their wide range of uses includes safety and insulation products, food and materials packaging, clothing and tools. Specific polymers with qualities such as biodegradability, biocompatibility or electro active properties find uses in more specialized and demanding applications.

This research focuses on a functional polymeric material, polyvinylidene fluoride (PVDF or PVF<sub>2</sub>). Due to its unique piezoelectric properties, flexibility, and light weight it is one of the most favored candidates for miniature applications. This research investigates the application of thin-film PVDF in miniature deflection sensors used for studying the locomotion of small insects. A laboratory system is designed and set up to test the sensors in detail. The following chapters discuss the background information of sensors, experimental setup, and initial analysis of cockroach's behavior.

---

This thesis follows the style of Journal of Applied Physics.

## I.1 History of piezoelectricity

Piezoelectricity is defined as the ability of certain materials to generate electrical charge due to mechanical deformation. The name comes from an ancient Greek word *piezein* meaning to ‘squeeze’ or ‘press’. It was first discovered in 1880 by the brothers Pierre and Jacques Curie, who demonstrated piezoelectricity in various crystals including zincblende, tourmaline, cane sugar, topaz, and quartz.<sup>1</sup> Within a year, a converse piezoelectric effect was predicted by Lippmann based on thermodynamic considerations. This behavior was also confirmed by the Curies.<sup>2</sup>

The first practical applications came a few decades later. In 1918, Langevin developed an ultrasonic submarine detection technique using a quartz-based piezoelectric transducer.<sup>3</sup> This approach, known as sonar, was subsequently used during both world wars. It is also generally accepted that the use of quartz for stabilization of oscillators in the 1920s initiated the field of frequency control.<sup>4</sup>

Further developments in piezoelectricity took place in the 1950s and 1960s when studies focused on polymers and their properties. In 1969, Kawai discovered strong piezoelectric properties in polyvinylidene fluoride.<sup>5</sup> This breakthrough resulted in huge wave of interest in research and applications of this material.

## I.2 Introduction to the polyvinylidene fluoride (PVDF)

Polyvinylidene fluoride is a long-chain polymer consisting of many identical repeat units (monomers). Each unit is a  $\text{CF}_2\text{CH}_2$  molecule shown in Figure 1.

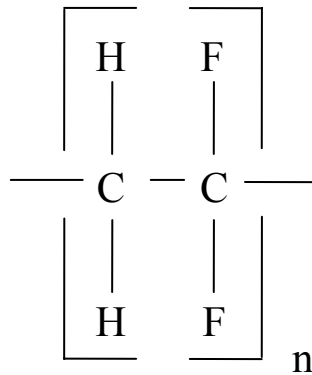


**Figure 1 Polyvinylidene fluoride molecule.**

These elementary repeat units are chemically linked to create chains during the polymerization process. The molecular weight of PVDF is about 100,000 g/mol corresponding to 2,000 monomers or an extended length of  $0.5 \times 10^{-4}$  cm (0.5  $\mu\text{m}$ ).<sup>6</sup> The molecules are highly polar due to the negatively charged fluoride and positively charged hydrogen atoms.<sup>7</sup> Each monomer unit has a dipole moment of  $7.56 \times 10^{-30}$  C-m or 2.27 D.<sup>8</sup>

The three main conformations of polyvinylidene fluoride are the all-trans (planar zigzag) form I ( $\beta$  phase), the trans-gauche-trans-gauche' (TGTG') form II ( $\alpha$  phase), and the T3GT3G' form III ( $\gamma$  phase).<sup>9,10,11,12</sup> Additional variations (including  $\delta$  phase) can be obtained at specific temperature and poling conditions.<sup>13,14</sup> The polymer structures are normally identified and studied using infrared transmission and x-ray scattering techniques.<sup>8</sup> Figure 2 shows schematics of the two most common PVDF conformations, the  $\alpha$  and  $\beta$  phases, with the chain axis oriented in the vertical direction.

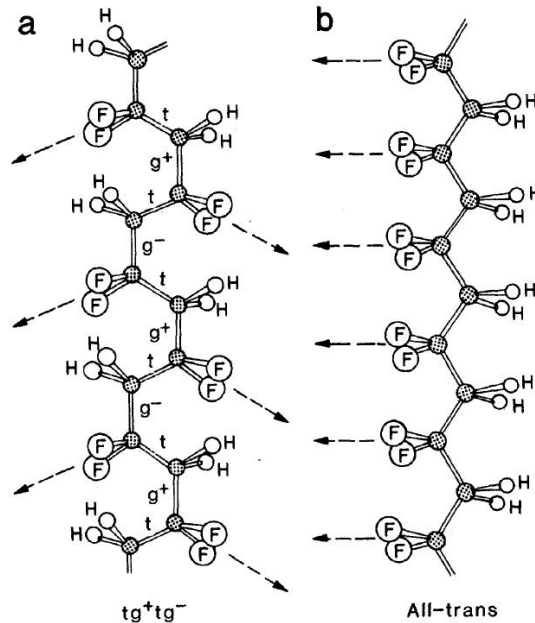


**Figure 2** Diagrams of (a)  $\alpha$ -phase and (b)  $\beta$ -phase chain conformations in PVDF. (Lovinger 1983). Reprinted with permission from AAAS.<sup>15</sup>

The dipole directions are indicated with arrows in the above diagram. In the  $\alpha$ -phase they are pointed in opposing directions, resulting in partial dipole cancellation and a nearly non-polar structure. The  $\beta$ -phase exhibits consistent dipole orientations perpendicular to the molecular axis. Due to the regular alignment of all molecules, the all-trans is the most polar conformation of PVDF ( $7.0 \times 10^{-30}$  C-m or 2.1 D per repeat unit) resulting in the highest piezoelectric properties.<sup>8,15</sup> Other conformations, such as the  $\gamma$  and  $\delta$  phases are also slightly polar, however their piezoelectric properties are much lower.

In a melt form, PVDF molecular chains have no fixed structure and can move around freely. When cooled, the melt solidifies, crystallizing into spherulites – spherical pockets growing outward from the nucleation point.<sup>16</sup> Material obtained in this way typically consists of chains in the  $\alpha$  and  $\gamma$  phase conformations.<sup>17,18</sup> Achieving  $\beta$  phase



structures normally requires additional processing as discussed later in the manufacturing section. A microscope image of PVDF crystallized from melt is shown in Figure 3.

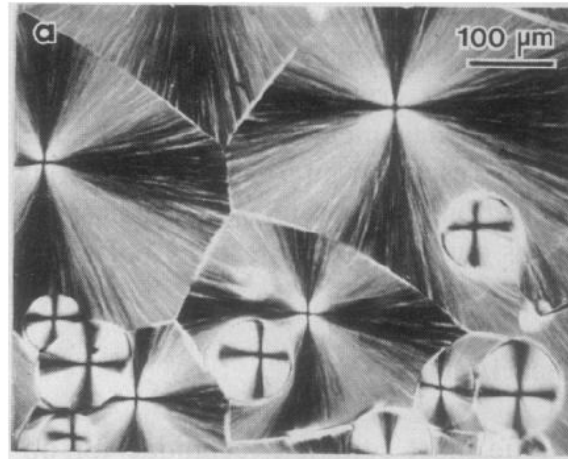


**Figure 3** Polarizing microscope image of PVDF spherulites. (Lovinger 1983). Reprinted with permission from AAAS.<sup>15</sup>

The radial structures of the  $\alpha$  and  $\gamma$  phase spherulites are visible (larger and smaller ones respectively) above. The dark crosses are due to the optical polarization of the microscope. A schematic representation of spherulite structures is presented in Figure 4.

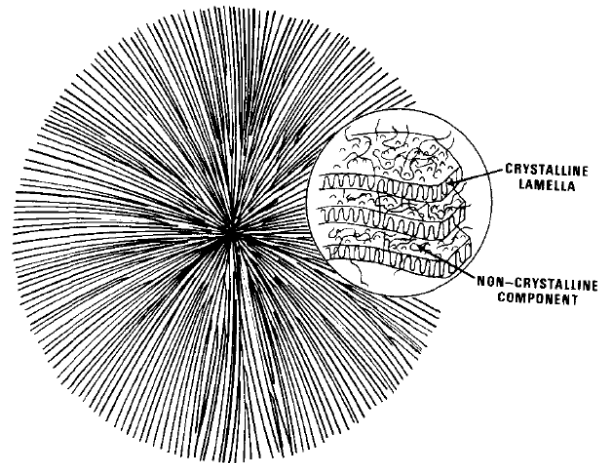


**Figure 4 PVDF spherulite structure diagram.**<sup>7</sup>

PVDF never crystallizes completely and as shown in this diagram both crystalline lamella structures and amorphous regions are present. The radial fibers, also visible in an earlier microscope image (Figure 3) consist of very thin, platelet-like crystals called lamellae separated by amorphous regions. The lamellae are segments of polymer chains packed in a crystalline order. They are on the order of a few nanometers thick and several micrometers in lateral dimensions.<sup>8,15</sup> The lamellae are surrounded by an amorphous structure also known as supercooled liquid phase due to its physical properties. Each PVDF molecule normally extends through several crystalline and amorphous regions. This two-phase solid state structure is typical of crystallizable polymers.<sup>15</sup>

The degree of crystallinity in PVDF ranges within 50-65% according to specific volume calculations.<sup>19</sup> This value varies slightly depending on material thermal history and the amount of chain ordering defects.<sup>20</sup> Chain defects are head-to-head ( $\text{CH}_2$  followed by  $\text{CH}_2$ ), and tail-to-tail ( $\text{CF}_2$  followed by  $\text{CF}_2$ ) bonds which occur during

polymerization. They are found in less than five percent of the sequences as shown by nuclear magnetic resonance spectroscopy studies.<sup>15</sup>

Due to physical characteristics of the material, piezoelectric properties are limited to certain temperature ranges. They vanish temporarily below the PVDF glass temperature  $T_g$  ( $-40^\circ\text{C}$ ). Also, when temperature rises beyond the Curie temperature  $T_c$  ( $80^\circ\text{C}$ ) the piezoelectric properties are lost permanently due to structural changes in the material.<sup>21</sup>

### I.3 Piezoelectric behavior overview

PVDF belongs to a group of piezoelectric materials which also display an additional property known as pyroelectricity. It is the ability to generate an electrical charge with temperature change. This behavior is due to the permanently polar structure of the material. In addition to being polar, some pyroelectric materials can have their spontaneous polarization axis reoriented or reversed with the application of an electric field. These materials are referred to as ferroelectric.<sup>15</sup> The name is derived by analogy with ferromagnetism, where the individual atoms exhibit permanent magnetic moments.<sup>22,23</sup>

It was initially uncertain whether PVDF is truly ferroelectric. Studies have shown inhomogeneous polarization across the film thickness, with higher polarization on the positive electrode charge. This led to speculations that the PVDF properties were due to trapped charges injected by the electrodes.<sup>23,24</sup> The dilemma was resolved when X-ray studies showed that polarization anisotropy disappears at high poling fields, and that ferroelectric dipole reorientation can be achieved.<sup>25</sup> Polarization reversal was further

attributed to dipole rotation using infrared techniques.<sup>26</sup> Typical ferroelectric hysteresis loops and Curie transitions were also shown to exist in this material.<sup>15</sup> PVDF is therefore considered to be a ferroelectric polymer.

There remains some uncertainty about the basic mechanism responsible for piezoelectricity in PVDF. Given its semi-crystalline structure, PVDF is modeled as a two-phase matrix with varied properties.<sup>7,27</sup> Piezoelectric response is dependent on polarization (average dipole moment per unit volume), which can be affected by changes in either dipole moment or volume.<sup>7</sup> A diagram in Figure 5 shows crystalline lamellar structure of PVDF.

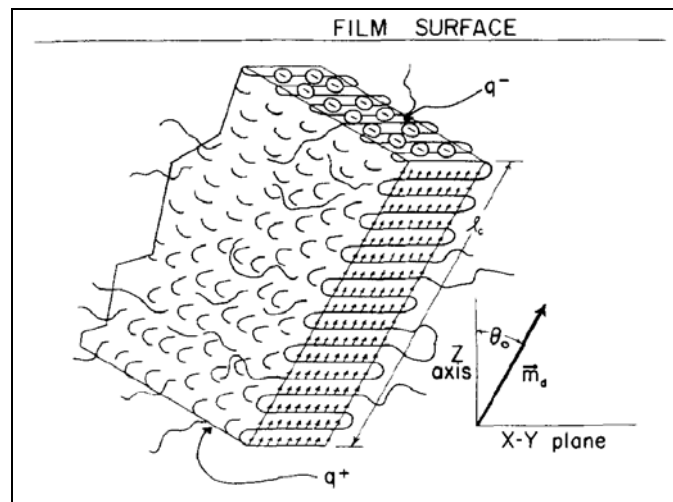


**Figure 5 Diagram of a PVDF lamellar crystal and its dipole orientation.<sup>7</sup>**

The dipole moment  $m_d$  and its angle  $\theta_0$  in relation to direction normal to the surface are shown for reference. The material's polarization and piezoelectric response are therefore affected by density of crystals (and hence crystallinity)<sup>28</sup> and their mean orientation.

As summarized by Broadhurst and Davis,<sup>6</sup> there are four essential elements to piezoelectricity: (a) the presence of permanent molecular dipoles; (b) the ability to orient or align the molecular dipoles; (c) the ability to sustain the dipole alignment achieved; and (d) the ability of the material to undergo large strains when mechanically stressed.

#### I.4 Piezoelectric mechanism research

A number of different approaches for explaining the piezoelectric effect have been explored over the years. After an initial debate regarding the influence of trapped space charges, scientists now agree that while space charges do attribute to the material's properties, their effect is negligible as over 90% of piezoelectric response occurs due to polarization of dipoles in crystalline areas.<sup>8,28,29</sup>

Some researchers propose that due to the dipole alignment and high compressibility of PVDF, large polarization changes can occur through changes in volume,<sup>4,30,31</sup> especially through thickness changes (also known as dimensional effect).<sup>28</sup> Other theoretical mechanisms are based on changes in moment, including Ohigashi's proposed dipole alignment increase due to mechanical stress.<sup>32</sup> Most studies agree that PVDF should be modeled as a two-phase matrix of crystalline and amorphous phases with different mechanical and dielectric properties.<sup>7,33,34</sup> It is then believed that the piezoelectric effect is due to mechanical and electrical interaction between crystalline and amorphous phases.<sup>27</sup> The specific examples of piezoelectricity sources in two-phase materials can be explained as follows:<sup>34</sup>

(a) The intrinsic piezoelectricity of crystalline elements creates the piezoelectricity due to the strain dependence of the polarization (crystal contribution).

(b) The relationship between the dielectric constants and strain is different between the crystalline and amorphous phases. With the presence of polarization these differences add to the piezoelectric effect in the material (electrostrictive contribution).

(c) The elastic constants of the crystalline and amorphous regions are also different. In a polarized sample, the resulting strain dependence of the polarization contributes to the piezoelectric activity (dimensional contribution).

This concludes the overview of existing studies of piezoelectricity in PVDF. The following section presents the general mathematical formulations used to describe this phenomenon.

## I.5 General piezoelectric equations

Piezoelectricity is a coupling mechanism relating material's mechanical and electrical properties, as outlined in Figure 6.

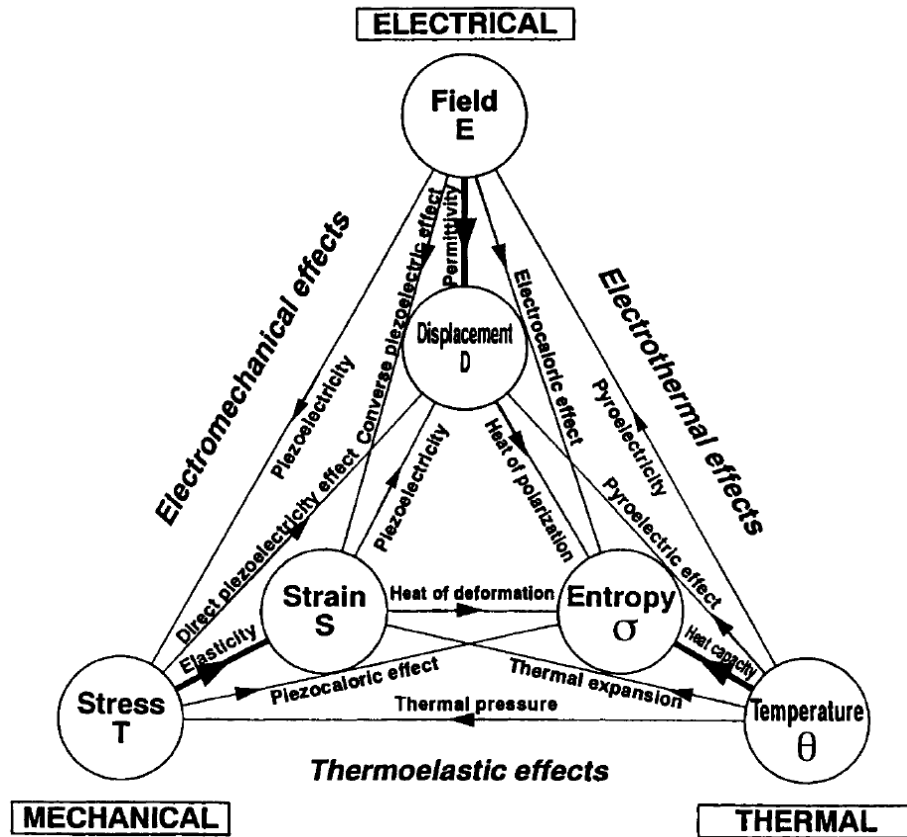
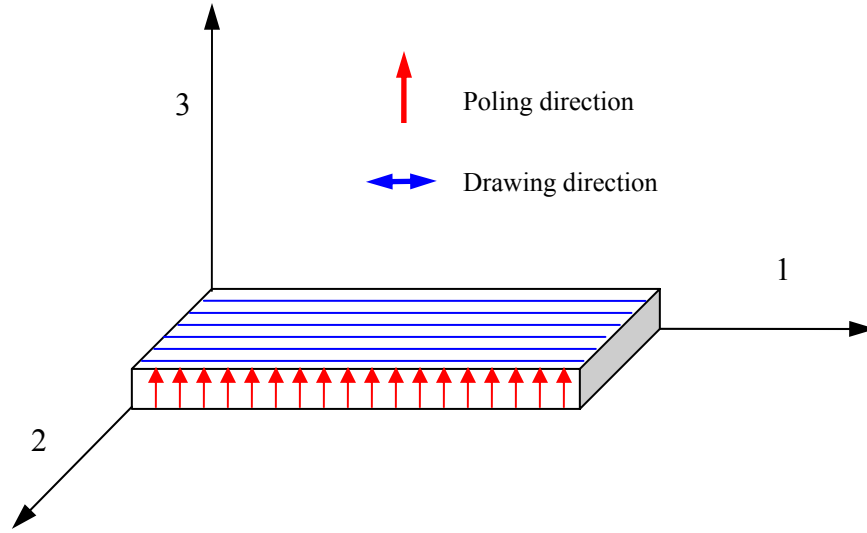


Figure 6 Relationships among material properties.<sup>35</sup>

Constitutive relations describing the piezoelectric behavior in materials can be derived from thermodynamic principles.<sup>36</sup> A tensor notation is normally used to identify the coupling mechanisms. It is common practice to label the axis directions as shown in Figure 7.



**Figure 7 Tensor directions for constitutive relation definitions.**

The mechanical drawing direction is labeled as "1". The "2" axis is the transverse direction in the plane of the sheet. The polarization axis (normal to film surface) is denoted as "3". Additional shear planes indicated by subscripts "4", "5", "6" are defined perpendicular to directions "1", "2", and "3" respectively.<sup>23</sup>

Piezoelectricity can be described by four constants  $d_{ij}$ ,  $e_{ij}$ ,  $g_{ij}$ , and  $h_{ij}$ . These constants relate elastic coefficients (mechanical stress  $T$  and strain  $S$ ) and dielectric variables (electric displacement  $D$  and electric field  $E$ ). The relationships are defined by the following formulas:<sup>28</sup>

$$d_{ij} = \left( \frac{\partial D_i}{\partial T_j} \right)^E = \left( \frac{\partial S_i}{\partial E_j} \right)^T \quad (1.1)$$

$$e_{ij} = \left( \frac{\partial D_i}{\partial S_j} \right)^E = - \left( \frac{\partial T_i}{\partial E_j} \right)^S \quad (1.2)$$



$$g_{ij} = -\left(\frac{\partial E_i}{\partial T_j}\right)^D = \left(\frac{\partial S_i}{\partial D_j}\right)^T \quad (1.3)$$

$$h_{ij} = \left(\frac{\partial E_i}{\partial S_j}\right)^D = \left(\frac{\partial T_i}{\partial D_j}\right)^S \quad (1.4)$$

The first two equations (1.1, 1.2) correspond to the direct piezoelectric effect, while the last two (1.3, 1.4) refer to the inverse piezoelectric effect. The superscripts describe the experimental conditions:  $E$  denotes zero electric field (a closed circuit),  $D$  stands for zero electric induction (an open circuit),  $T$  corresponds to zero mechanical stress (a free sample), and  $S$  indicates zero strain (a fixed sample). The subscripts are  $i = 1-3$  and  $j = 1-6$ . The above piezoelectric constants are related to each other through the elastic constant ( $c$ ) and dielectric constant ( $\epsilon$ ), can be calculated as.<sup>23,28</sup>

$$c = \frac{e}{d} = \frac{h}{g} \quad (1.5)$$

$$\epsilon\epsilon_0 = \frac{d}{g} = \frac{e}{h} \quad (1.6)$$

where  $\epsilon_0 = 8.854 \times 10^{-12}$  (F/m) is the permittivity of vacuum. The permittivity of piezoelectric materials depends on the boundary conditions. The free ( $dT = 0$ ) permittivity  $\epsilon^T$  is always larger than the clamped ( $dS = 0$ ) permittivity  $\epsilon^S$  because a free sample piezoelectric generates additional polarization due to converse and direct piezo effects. Similarly, the open-circuit ( $dD = 0$ ) elastic constant  $c^D$  is larger than the short-circuit ( $dE = 0$ ) constant  $c^E$ . The above dependences define the electromechanical coupling coefficient  $k$  as:<sup>23,28</sup>

$$\frac{\epsilon^S}{\epsilon^T} = \frac{c^E}{c^D} = 1 - k^2 \quad (1.7)$$

where  $k^2$ , which is always less than 1, represents the conversion of electrical energy into mechanical energy and vice versa due to piezoelectricity.

$$k^2 = \frac{\text{electrical energy converted to mechanical energy}}{\text{input electrical energy}}$$

$$k^2 = \frac{\text{mechanical energy converted to electrical energy}}{\text{input mechanical energy}} \quad (1.8)$$

The focus of this application is on linear piezoelectricity, which is described in the following section.

### I.6 Linear piezoelectricity

The linear constitutive relationships for piezoelectricity are defined using strain ( $S$ ), stress ( $T$ ), electric field ( $E$ ), and electric displacement ( $D$ ) as follows:<sup>37</sup>

$$S_j = s_{ji}^E T_i + d_{jm} E_m$$

$$D_m = d_{mj} T_j + \varepsilon_{km}^E E_k \quad (1.9)$$

which can be also written in the matrix form where electric displacement vector  $D$  ( $C/m^2$ ) is of size  $(3 \times 1)$ , the strain vector  $\varepsilon$  is  $(6 \times 1)$  (units dimensionless), the applied electric field  $E$  (V/m) is a  $(3 \times 1)$  and the stress  $T$  ( $N/m^2$ ) is a  $(6 \times 1)$  vector. The constants include the dielectric permittivity  $\varepsilon_{km}^E$  (F/m)  $(3 \times 3)$  matrix, the piezoelectric coefficients  $d_{jm}$   $(3 \times 6)$  and  $d_{mj}$   $(6 \times 3)$  (C/N or m/V), and the elastic compliance matrix  $s_{ji}^E$  of size  $(6 \times 6)$  ( $m^2/N$ ). The piezoelectric coefficient  $d_{jm}$  (m/V) defines strain per unit field at constant stress and  $d_{mj}$  (C/N) defines electric displacement per unit stress at constant electric field. Hence the matrix notation of equation (1.9) above is:<sup>38</sup>

$$\begin{bmatrix} S_1 \\ S_2 \\ S_3 \\ S_4 \\ S_5 \\ S_6 \end{bmatrix} = \begin{bmatrix} d_{11} & d_{12} & d_{13} \\ d_{21} & d_{22} & d_{23} \\ d_{31} & d_{32} & d_{33} \\ d_{41} & d_{42} & d_{43} \\ d_{51} & d_{52} & d_{53} \\ d_{61} & d_{62} & d_{63} \end{bmatrix} \begin{bmatrix} E_1 \\ E_2 \\ E_3 \end{bmatrix} + \begin{bmatrix} S_{11}^E & S_{12}^E & S_{13}^E & S_{14}^E & S_{15}^E & S_{16}^E \\ S_{21}^E & S_{22}^E & S_{23}^E & S_{24}^E & S_{25}^E & S_{26}^E \\ S_{31}^E & S_{32}^E & S_{33}^E & S_{34}^E & S_{35}^E & S_{36}^E \\ S_{41}^E & S_{42}^E & S_{43}^E & S_{44}^E & S_{45}^E & S_{46}^E \\ S_{51}^E & S_{52}^E & S_{53}^E & S_{54}^E & S_{55}^E & S_{56}^E \\ S_{61}^E & S_{62}^E & S_{63}^E & S_{64}^E & S_{65}^E & S_{66}^E \end{bmatrix} \begin{bmatrix} T_1 \\ T_2 \\ T_3 \\ T_4 \\ T_5 \\ T_6 \end{bmatrix} \quad (1.10)$$

$$\begin{bmatrix} D_1 \\ D_2 \\ D_3 \end{bmatrix} = \begin{bmatrix} \mathcal{E}_{11}^T & \mathcal{E}_{12}^T & \mathcal{E}_{13}^T \\ \mathcal{E}_{21}^T & \mathcal{E}_{22}^T & \mathcal{E}_{23}^T \\ \mathcal{E}_{31}^T & \mathcal{E}_{32}^T & \mathcal{E}_{33}^T \end{bmatrix} \begin{bmatrix} E_1 \\ E_2 \\ E_3 \end{bmatrix} + \begin{bmatrix} d_{11} & d_{12} & d_{13} & d_{14} & d_{15} & d_{16} \\ d_{21} & d_{22} & d_{23} & d_{24} & d_{25} & d_{26} \\ d_{31} & d_{32} & d_{33} & d_{34} & d_{35} & d_{36} \end{bmatrix} \begin{bmatrix} T_1 \\ T_2 \\ T_3 \\ T_4 \\ T_5 \\ T_6 \end{bmatrix} \quad (1.11)$$

For a thin film, the piezoelectric constant  $d_{jm}$  is expressed in terms of axis directions defined in Figure 7 earlier. The  $d_{jm}$  matrix is therefore expressed as:<sup>23,38</sup>

$$d = \begin{bmatrix} 0 & 0 & d_{31} \\ 0 & 0 & d_{32} \\ 0 & 0 & d_{33} \\ 0 & d_{24} & 0 \\ d_{15} & 0 & 0 \\ 0 & 0 & 0 \end{bmatrix} \quad (1.12)$$

where, for each coefficient, the first subscript is the poling direction and the second one is that of the mechanical deformation or stress.<sup>15,23</sup> Due to the poling orientation and the limited thickness of the film, its piezoelectricity is limited to a few directions, with zero coefficients in the remaining axis. The main coefficients of interest  $d_{31}$ ,  $d_{32}$  and  $d_{33}$  relate the normal strain in the “1”, “2” and “3” directions respectively to the poling direction normal to the film surface.<sup>38</sup> The piezoelectric constant along the drawing or molecular direction  $d_{31}$  is an order of magnitude greater than that transverse to

the polymer chains  $d_{32}$ . Both are positive, since stress in the film plane reduces the specimen thickness, thus increasing the surface charge. The  $d_{33}$  coefficient is negative because a stress normal to the film increases its thickness.<sup>15</sup> Additional coefficients  $d_{15}$  and  $d_{24}$  represent the shear strain in the 1-3 plane and the 2-3 plane respectively.<sup>38</sup> They arise from anisotropy due to texturing created by mechanical elongation during material processing.<sup>28,38,39,40,41</sup> Individual piezoelectric constants can be determined through resonance studies using direct and converse effects, or calculated if other piezoelectric constants are already known.<sup>23,28,42</sup> For most sensor applications, the  $d_{31}$  (transverse effect) and  $d_{33}$  (longitudinal effect) components are of primary importance.<sup>28</sup>

In this research, the electrical charge generation due to mechanical deflection is studied experimentally. Charge build-up is normally only seen while deflection is changing. In a static condition, it dissipates through the PVDF film and the measuring equipment. A simplification is made for the purpose of further mathematical analysis of this study. Since it is not possible to analyze piezoelectric materials in purely static conditions due to coupling between electrical and dynamic mechanical variables, quasi-static conditions are considered instead. This is possible, because full electromagnetic equations can be neglected in the piezoelectric behavior considerations, as the magnetic effects are known to be significantly smaller than the electrical effects.<sup>37</sup> In addition, the external applied electric field  $E$  is zero, simplifying the piezo relations further.

Therefore, the relevant piezoelectric equation becomes:

$$D_m = d_{mj}T_j \quad (1.13)$$

or in the matrix form:<sup>38</sup>

$$\begin{bmatrix} D_1 \\ D_2 \\ D_3 \end{bmatrix} = \begin{bmatrix} 0 & 0 & 0 & 0 & d_{15} & d_{16} \\ 0 & 0 & 0 & d_{24} & 0 & 0 \\ d_{31} & d_{32} & d_{33} & 0 & 0 & 0 \end{bmatrix} \begin{bmatrix} T_1 \\ T_2 \\ T_3 \\ T_4 \\ T_5 \\ T_6 \end{bmatrix} \quad (1.14)$$

where the stress vector is defined as:

$$\begin{bmatrix} T_1 \\ T_2 \\ T_3 \\ T_4 \\ T_5 \\ T_6 \end{bmatrix} = \begin{bmatrix} T_{11} \\ T_{22} \\ T_{33} \\ T_{23} \\ T_{31} \\ T_{12} \end{bmatrix} \quad (1.15)$$

The electric displacement  $D$  is related to the charge generated by the following relation.<sup>38</sup>

$$q = \iint [D_1 \quad D_2 \quad D_3] \begin{bmatrix} dA_1 \\ dA_2 \\ dA_3 \end{bmatrix} \quad (1.16)$$

where  $dA_1$ ,  $dA_2$  and  $dA_3$  are the components of the electrode area in the 2-3, 1-3 and 1-2 planes respectively. Therefore, the generated charge  $q$  depends only on the component of the displacement  $D$  normal to the electrode area  $dA$ .<sup>38</sup> It is worth noting that a pair of parallel electrodes is needed to measure piezoelectric charge. If shaped electrodes are used on each side of the film,  $dA$  consists only of the area where electrodes overlap.<sup>21</sup> This concludes the summary of the piezoelectric effect for this study.

## I.7 Manufacturing processes

This section presents an overview of the manufacturing process for the piezoelectric PVDF. The polymer can be synthesized from gaseous vinylidene fluoride (VDF) monomer through a free radical polymerization. It can be then formed into sheets through melt casting, or processing from a solution (e.g. solution casting, spin coating, and film casting). Depending on the processing method, various chain conformations of PVDF films may result.<sup>8,43,44</sup> Additional steps are necessary to obtain the piezoelectric properties within the material. Most common manufacturing techniques start with a slow melt casting process, resulting in an  $\alpha$  phase material. Additional steps are then taken to achieve the desired piezoelectric properties. Step-by-step methods are presented Figure 8.

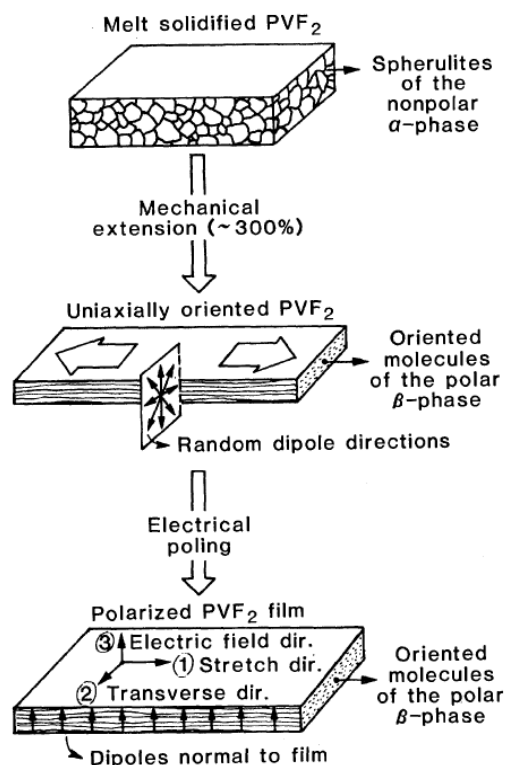


**Figure 8** PVDF manufacturing process. (Lovinger 1983). Reprinted with permission from AAAS.<sup>15</sup>

The PVDF melt is first subjected to mechanical drawing. This breaks the spherulite formations into polymer crystallites aligned in the direction of the force. When this deformation takes place at low temperatures (below 90°C), the polymer chains are not able to move freely and become distorted, achieving most extended molecular form, which is the desired  $\beta$  phase conformation.<sup>15</sup> Both uniaxial and biaxial drawing techniques may be applied with various elongation ratios (up to 700%).<sup>8,45,46,47</sup> At this point, the molecular dipoles are still randomly oriented, resulting in zero net polarization. An electric field normal to the material surface is applied to align the dipoles and create uniform material polarization. This can be accomplished through plasma or corona poling or the use of electrodes evaporated onto the film.<sup>48,49</sup> Poling conditions such as

field strength, temperature and poling time can vary, although increased values don't necessarily guarantee higher resulting piezoelectricity.<sup>28</sup> This completes the process and gives PVDF piezoelectric properties, making into a useful electroactive polymer.

The microstructure changes in PVDF during drawing and poling processes are further illustrated in Figure 9.

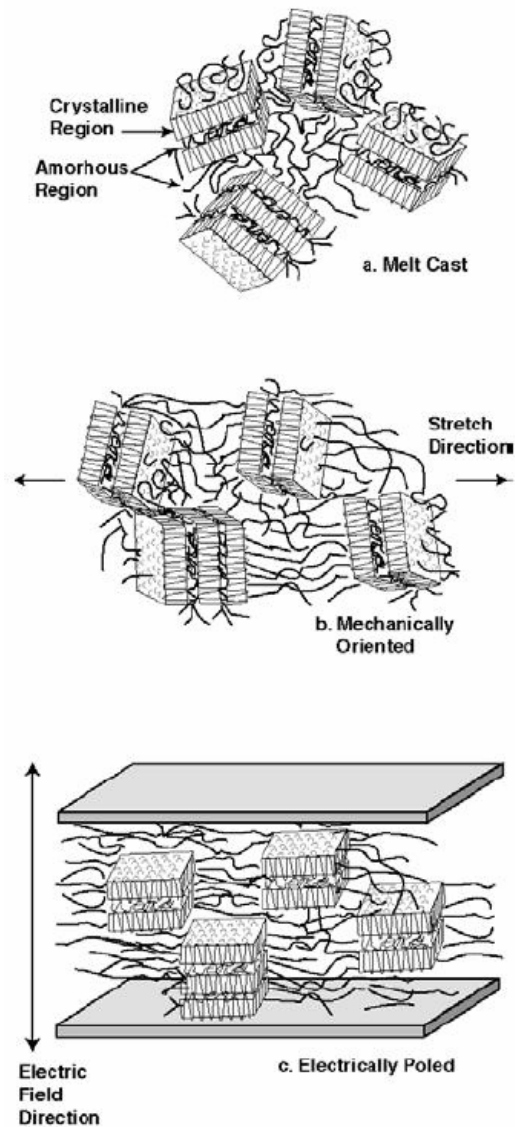


**Figure 9** Crystal lamellae and amorphous regions within PVDF: (a) melt cast; (b) structure alignment through mechanical stretching; (c) lamellae oriented due to electrical poling.<sup>23</sup>



Figure 9(a) shows the randomly oriented crystalline and amorphous structures found in the polymer melt. Mechanical drawing extends the crystals into the polar  $\beta$  phase conformation and orients them as shown in Figure 9(b). Finally, through electrical poling the crystalline lamellae are aligned in a single direction as shown in Figure 9(c), resulting in a uniformly polar material with piezoelectric properties.

There are a number of other polymers that can be made piezoelectric,<sup>35</sup> however PVDF exhibits by far the strongest piezoelectric and pyroelectric properties.<sup>15</sup> As described earlier, the piezoelectric properties are dependent on its molecular form, level of crystallinity and the poling process. Since the discovery of piezoelectricity in PVDF in 1969, its piezoelectric constants have increased about six times due to process advancements. Further progress can be expected, however dramatic future improvements are not likely.<sup>8</sup>

## I.8 Applications

Polyvinylidene fluoride is a well known commercial material with many useful characteristics and a wide range of applications. Some of its most important properties include: high purity, resistance to weather and chemicals, light weight, mechanical strength and abrasion resistance. It's thermoplastic and can be easily processed into various shapes. Non-piezoelectric PVDF, marketed as Kynar®, finds uses in pipes and chemical storage tanks, coating and paint additives, electrical wire jacketing, battery components and other products.<sup>50</sup>

Piezoelectric PVDF is commonly used for sensors, actuators and transducers. Its key benefits in these applications include: high voltage sensitivity, flexibility, toughness

and manufacturability. It can be made biocompatible and its low acoustic impedance is close to that of water, making it useful for fluid sensors and biomedical applications.<sup>23,51</sup> An full list of commercial and research applications includes: strain and strain rate gauges<sup>21</sup>; potential active biomedical materials<sup>52,53</sup>; switches, impact and vibrations sensors, accelerometers<sup>54,55</sup>; flow detectors<sup>47</sup>; devices in acoustics, ultrasonics and vibration control.<sup>54,56,57,58</sup> In summary, piezoelectric PVDF has many uses in sensing and actuating applications. In this study, it is utilized as a deflection sensor. The application details are discussed in the following section.

## I.9 Motivation and objectives

A detailed introduction to piezoelectric materials has been presented in previous sections to provide a solid background of the topic. This research focuses on the use of PVDF as a deflection sensor to monitor small insects, such as cockroaches. Using piezoelectric polymers to study insects has significant importance in the fields of biology, engineering, and science. This research uses an experimental approach combined with simple analytical techniques to develop, test, and optimize PVDF sensors for monitoring cockroaches.

For decades, understanding and mimicking insect locomotion has been the focus of numerous studies.<sup>59,60</sup> The goal has often been learning about the connection between muscle activity and movement, leading to the development of motion simulations and models.<sup>61,62,63,64</sup> Another popular area of research is animal monitoring. A wide variety of technological devices have been developed to observe and study insects remotely without direct interference.<sup>65</sup> This area of research, known as “wildlife telemetry” has

gained additional momentum through miniaturization of data transfer devices for the use with small animals and insects.<sup>66,67,68,69,70</sup> Roaches in particular have been an interest of many studies, because they are common and inherently related to people and their environments.

For this research a discoid roach, *Blaberus discoidalis* is used. It is a neotropical species that is easy to rear and useful as a biological insect model. The roaches, shown in Figure 10, are about 40 mm long, which makes them relatively easy to handle.



**Figure 10** Discoid roach (*Blaberus discoidalis*) – relative size (L-female, R-male).<sup>71</sup>

Roaches are found almost every place where there is food and moisture.<sup>72,73,74</sup> They are omnivorous, preferring to sweets but also found eating a variety of commercial and household foods and materials.<sup>62,65</sup> There are several reasons to study the *Blaberus discoidalis*. This species, as any other roach, has a simple biological structure are easy to obtain and maintain. Long-term monitoring of roaches' behavior and their appetite allows the analysis of their food structure and agriculture distribution, which have a significant impact on environmental studies.

## I.10 Approaches

An experimental approach was taken for the initial phase of the project focused on developing miniature, robust sensors and dependable testing platforms for both laboratory and roach experiments. Results of initial tests, along with basic analytical considerations, were used to improve the performance and reliability of the sensors and the testing setups. Experiments were then carried out to characterize the relationship between the cockroach movements and the sensor response to further the understanding of insect behavior.

This research presents a set of interesting engineering challenges. The main difficulty is the miniature size of the application, which limits the techniques available for sensor synthesis and mounting. The process of selecting a sensor attachment method has shown that the most reliable approach results in the piezoelectric film undergoing a buckling deformation during insect movement. While PVDF film has been studied extensively, most of the research to date focused on its behavior in stretching or bending applications. The difference between them is shown in Figure 11.

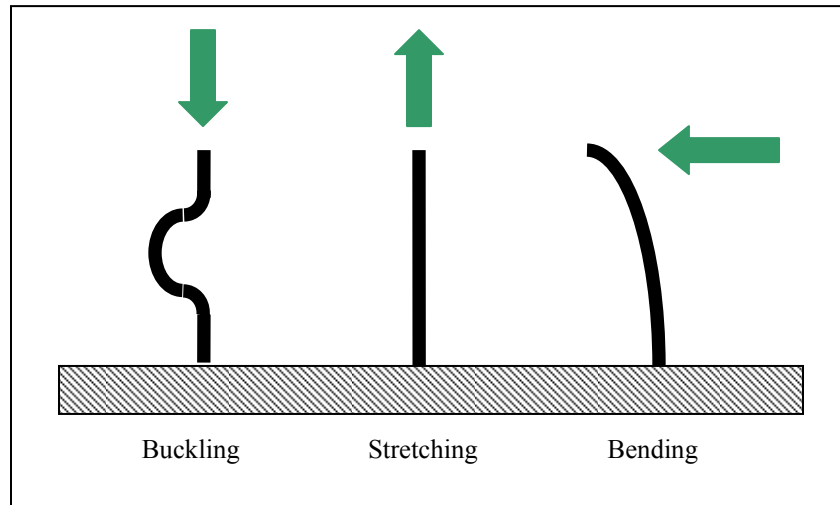


**Figure 11 Buckling, stretching and bending deflections.**

Buckling deflections and stresses are different from those in bending and a separate set of constraints must be considered. Additionally, because buckling is a mechanically unstable condition, exact solutions often cannot be found and approximations must be used instead, as discussed in the results section of this document.

In summary, the experimental approach discussed here can be divided into: sensor synthesis and experimental setup (roach testing and laboratory testing). Each one will be discussed in further detail in the following chapters.

## CHAPTER II

### SENSOR FABRICATION

This section presents a brief overview of the materials used, their preparation, assembly and implementation in the presented study.

#### II.1 Materials

Metallized piezoelectric film (Measurement Specialties, part number 1-1004346-1) was used for this study. It consists of a 28 $\mu$ m layer of PVDF with coatings of silver ink deposited on both sides (5-7  $\mu$ m each) to provide an electrical connection. Thin, insulated copper wires, 0.0047" (0.12 mm) in diameter, were used for electrical leads. Standard semi-clear adhesive scotch tape was used to assemble the sensors. Tools such as fine sandpaper (320 grain) for removing wire insulation, and scalpel blades for cutting sensor material were also used in the project.

#### II.2 Material properties

A summary of PVDF film characteristics, as provided by the manufacturer, are listed in Table 1:

Table 1 Properties of PVDF film.<sup>54</sup>

Symbol	Parameter		PVDF	Units
t	Thickness		9, 28, 52, 110	$\mu\text{m}$ (micron, $10^{-6}$ )
$d_{31}$	Piezo Strain Constant		23	$10^{-12} \frac{\text{m/m}}{\text{V/m}}$ or $\frac{\text{C/m}^2}{\text{N/m}^2}$
$d_{33}$			-33	
$g_{31}$	Piezo Stress constant		216	$10^{-3} \frac{\text{V/m}}{\text{N/m}^2}$ or $\frac{\text{m/m}}{\text{C/m}^2}$
$g_{33}$			-330	
$k_{31}$	Electromechanical Coupling Factor		12%	
$k_3$			14%	
C	Capacitance		380 for 28 $\mu\text{m}$	pF/cm <sup>2</sup> @ 1KHz
Y	Young's Modulus		2-4	$10^8 \text{ N/m}^2$
$V_0$	Speed of Sound	stretch:	1.5	$10^3 \text{ m/s}$
		thickness:	2.2	
p	Pyroelectric Coefficient		30	$10^{-6} \text{ C/m}^2 \text{ }^\circ\text{K}$
$\epsilon$	Permittivity		106-113	$10^{-12} \text{ F/m}$
$\epsilon/\epsilon_0$	Relative Permittivity		12-13	
$\rho_m$	Mass Density		1.78	$10^3 \text{ kg/m}$
$\rho_e$	Volume Resistivity		$>10^{13}$	Ohm meters
$R_{\square}$	Surface Metallization Resistivity		$<3.0$	Ohms/square for NiAl
$R_{\square}$			0.1	Ohms/square for Ag Ink
$\tan \delta_e$	Loss Tangent		0.02	@ 1KHz
	Yield Strength		45-55	$10^8 \text{ N/m}^2$ (stretch axis)
	Temperature Range		-40 to 80...100	$^\circ\text{C}$
	Water Absorption		$<0.02$	% H <sub>2</sub> O
	Maximum Operating Voltage		750 (30)	V/mil(V/ $\mu\text{m}$ ), DC, @ 25 $^\circ\text{C}$
	Breakdown Voltage		2000 (80)	V/mil(V/ $\mu\text{m}$ ), DC, @ 25 $^\circ\text{C}$

It is worth noting that mechanical properties such as Young's modulus and yield strength are generally given as a range, and not a specific value. This is because PVDF is a viscoelastic material. Its stress-strain response is time dependant, making it difficult to identify precisely. The polymer is sometimes assumed to be linearly viscoelastic, but only within certain stress levels.<sup>56</sup>

### II.3 Sensor synthesis

For the purpose of this work, commercially available thin piezoelectric PVDF film was used. The material is available from Measurement Specialties in various thicknesses (28, 52 and 110  $\mu\text{m}$ ). It is made using techniques similar to those described earlier in the manufacturing section (I.7). The piezoelectric film is then metallized through a process described in the next section. The application requires the sensors to be flexible and robust at the same time. After initial testing, the 28  $\mu\text{m}$  PVDF was chosen, because it provides little or no interference with the insects' movements. Its drawback is that it is easier to damage and its output signal is lower than that of thicker films. Complete details of sensor preparation are discussed in the following sections.

#### *II.3.1 Metallization*

For PVDF to be used as a sensor, a thin metal layer is deposited on each side of the film. This creates two electrodes and allows for measurement of the charge generated. Possible methods include screen printing with conductive silver ink. The resulting metallization layer is fairly thick (5-7  $\mu\text{m}$ ). This provides additional strength and improved durability, making the film more useful for mechanical applications. Silver ink metallization also provides good quality of the surface finish. It has a flat grey color and low reflectivity. A laser light used to measure sensor lateral deflection (as discussed in later chapters) doesn't reflect or scatter on this surface easily, allowing for more consistent readings.

Additional coating techniques are used including sputtering metallization, which results in thinner coating layers. Various metals and alloys can be deposited at a thickness around 500-700  $\text{\AA}$ . While this allows the film to be more flexible, the



metallization layer is not as robust and tends to crack due to repeated deformations.

Also, the surface is highly reflective, making it a less reliable target for the laser distance gauge.<sup>54,75</sup>

### *II.3.2 Sensor preparation*

Sensors are cut from PVDF film using a razor blade. Care must be taken not to stretch the material while cutting it. If the film becomes distorted, its two surface layers may come in contact, creating an electrical connection between them and making the sensor useless. Repeatable sensor sizes may also be difficult to achieve with a manual cutting process. Alternate, more reliable methods have been explored, such as custom punches to cut the piezoelectric film.<sup>76</sup> They may become useful in the future development of the project.

### *II.3.3 Lead attachment methods*

Wire leads are critical to the sensor operation, allowing the measurement of the generated signal. Thin 0.0047" (0.12 mm) copper wires with flexible electrical insulation are used. Insulation prevents accidental electrical "shorting" between the leads and is removed at the connection points with the sensor. Insulation removal can be challenging due to the small wire size. The most reliable solution found so far has been using fine sandpaper (320 grain) to remove the coating.

A number of wire attachment methods have been considered. Commercial solutions, such as penetrative techniques (piercing, riveting, crimping, etc) are not possible due to the miniature sensor dimensions and the need for patterned lead-off electrodes. The application and reliability of non-penetrative methods (low temperature soldering, conductive epoxies and adhesives) are also limited due to the sensor size.<sup>54</sup>

Simple wire attachments with adhesive scotch tape shown in Figure 12 have been found to be most effective. They are easy to implement and durable enough to meet the operating requirements of the sensor.

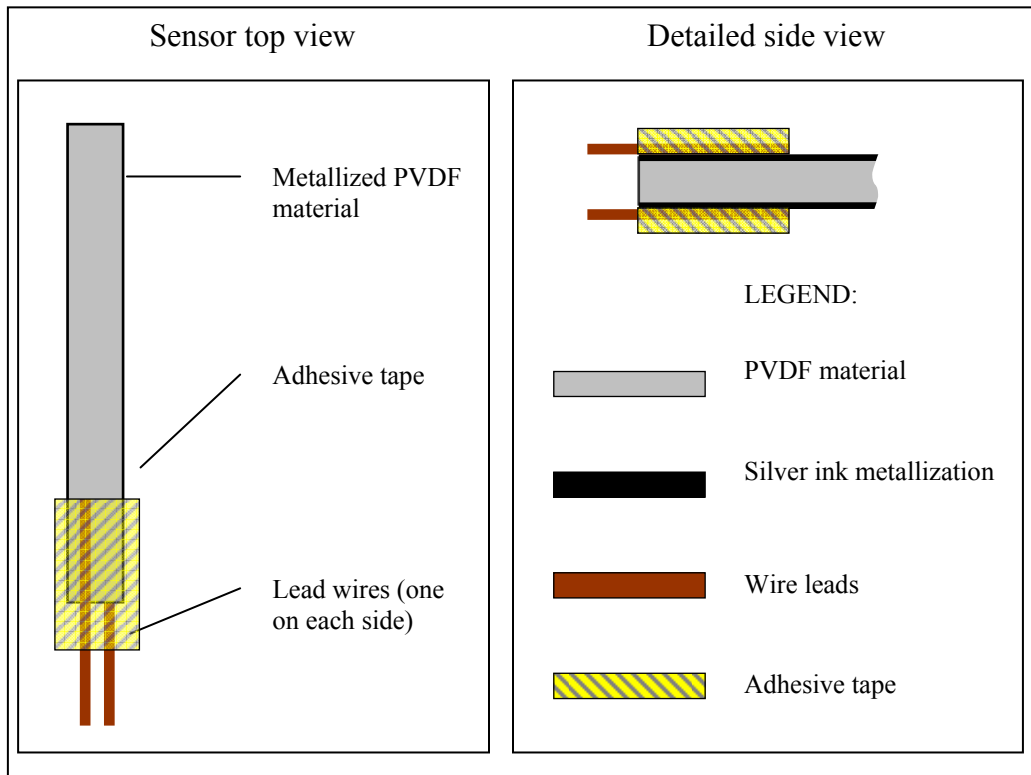


**Figure 12 Detailed sensor schematic.**

To provide a good electrical connection, wire insulation is removed over a length of about two millimeters from the end of each wire using sandpaper. The exposed leads are placed on each side of the sensor, slightly apart to avoid a possible connection between them. The sensor and wire leads are then “sandwiched” together between the two layers of tape as shown above. The wire attachment area is about 2 mm long and 1

mm across. The sensor itself is 10 mm long and 1 mm wide. An image of a complete sensor with a scale for size reference is shown in Figure 13.

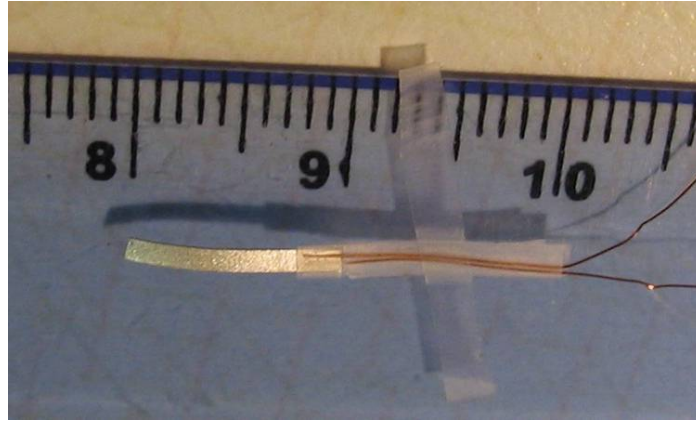


**Figure 13 Image of a complete sensor.**

The wires and their attachment points are limited in strength and easy to damage. The forces generated by insects are very small and it has been found that the sensors are fairly durable if handled with care. Possible improvements may be considered in later stages of the project.

#### II.4 Sensor mounting

The completed PVDF sensors were mounted on insects' legs to monitor their movements by measuring the generated charge. The piezoelectric sensor was attached to one of the metathoracic (rear) leg. Since those are the largest legs, they are easiest for sensor mounting, and also likely to generate highest forces and deflections. The attachment points are across the leg joints, one between the coxa and the femur (C-F), and another between the femur and the tibia (F-T) as shown in Figure 14.

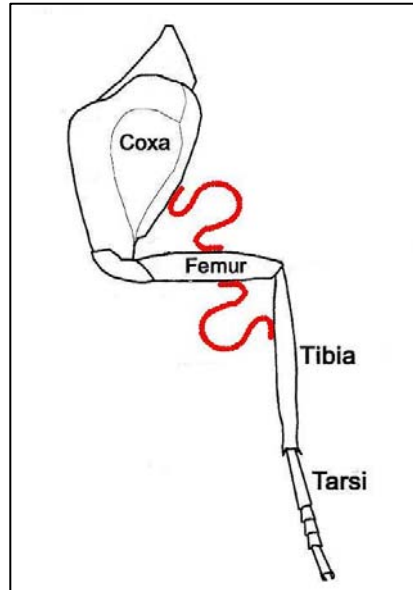


**Figure 14 Sensor locations across roach leg joints.<sup>62</sup>**

Narrow strips of thin elastic Parafilm® was used to attach the sensors. They were stretched and wrapped around the leg and over the ends of the sensor forming a strong bond between the PVDF strip and the roaches' cuticle. The coxae are thick and short, while the femur and tibia are fairly long and thin, making it relatively easy to attach the sensors to each of these leg parts. A fair amount of practice is necessary to perform this task. To prevent the insects from moving around during this process, they are temporarily placed in a small contained, which is then filled with carbon dioxide gas. This makes the cockroaches fall asleep, making them inactive for a short period of time. Figure 15 shows an image of the sensor attached on the roach's leg (F-T location).

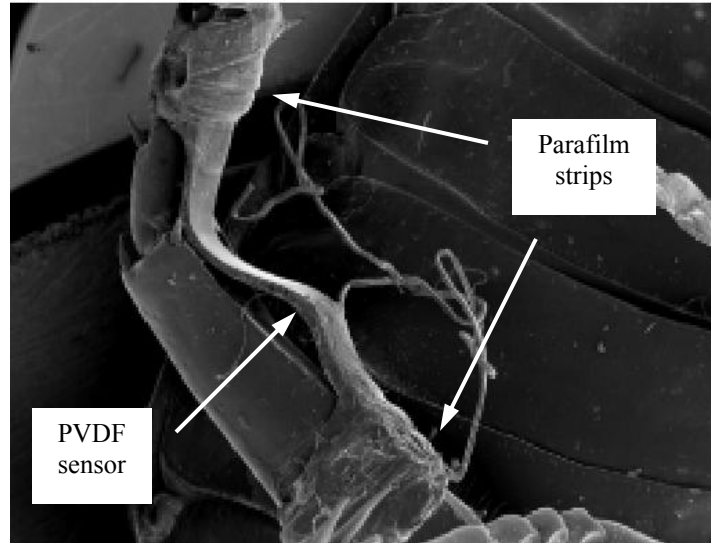


**Figure 15** Scanning electrode microscope (SEM) image of roach leg with a sensor.<sup>77</sup>

The sensor is thereby fixed to the leg with enough flexibility to deflect during insects' movements. The charge generated due to the film's piezoelectric properties can be measured and analyzed further. Details of the testing equipment and the experimental setup are presented in the next chapter.

## **CHAPTER III**

### **EXPERIMENTAL SETUP**

The experiments performed in this study can be grouped into sensor tests and material microstructure studies. Sensor experiment setups can be further divided into insect testing system and laboratory system.

#### III.1 Sensor testing background

Because the insect is a complex testing platform with limited control, it is useful to first develop a good understanding of sensor performance through studies in controlled environment, before trying to analyze data gathered from a live cockroach. It is important for the laboratory experimental setup to maintain similar mounting and operating characteristics found in the roach application. As discussed earlier in section I.10, the sensor deformation can be defined as buckling. This is further illustrated in Figure 16(a). The laboratory setup has the capability of creating similar sensor deflections, shown in Figure 16(b), under repeatable and precisely defined conditions.

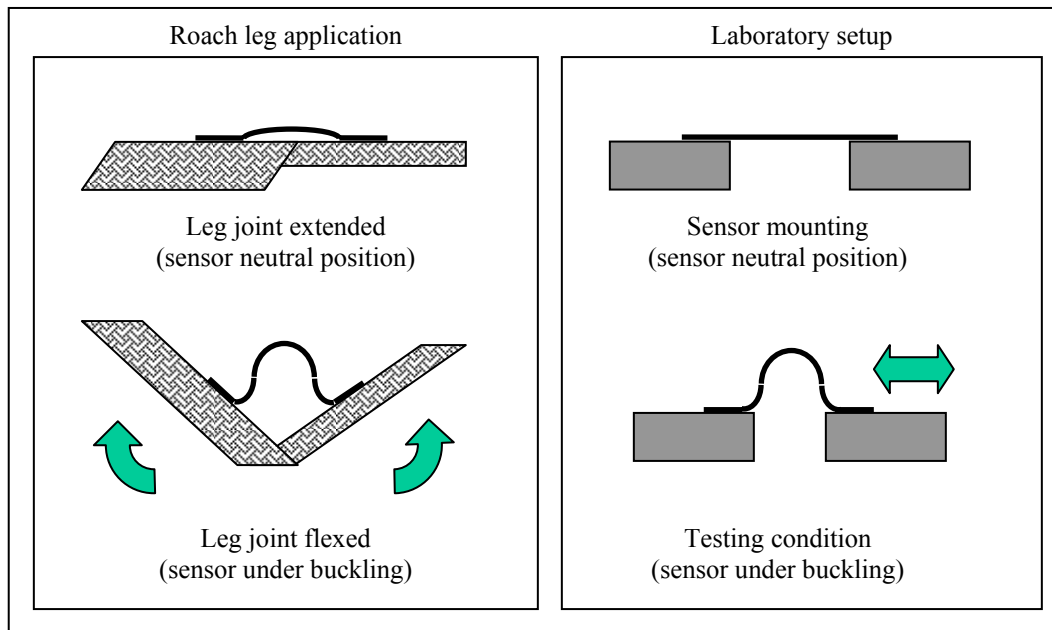


**Figure 16 Side-view schematic of sensor mounting and deformations – arrows indicate motion directions.**

In the experimental setup, the left mounting block is stationary, while the right one moves in the horizontal direction as shown by an arrow. The sensor buckling rate and deflection amplitude are directly controlled by the position of the movable fixture. Various motion paths can be defined, allowing the flexibility to generate various operating conditions. Simple motions can be implemented for studying the basic characteristics of the sensor. More complex deformations can be used to mimic real applications. Operating conditions of a sensor on an insect likely consist of a series of deflections, possibly of different amplitudes, occurring through across a range of frequencies. The roach is reported to be able to maintain sustained speeds at a rate up to 13 Hz.<sup>78</sup> Experiments performed so far were focused on lower deflection rates (below 10 Hz) to gain the basic understanding of the sensor and its operation. However, the

experimental system is capable of reaching the maximum frequencies expected during the roach motion.

### III.2 Insect testing setup

The testing setup allows monitoring the insect's leg movements while keeping the animal stationary. Once the PVDF sensor is attached to the roach's leg, the wires are routed along its back to prevent them from tangling with the other legs. The insect is attached to a permanent fixture by its wings as shown in Figure 17.



**Figure 17 Roach testing attachment. (Mika et al. 2007). Reprinted with permission from SPIE.<sup>79</sup>**

It is important to not to interfere with the roach's natural movements. The insect is given a lightweight styrofoam ball and through its natural reflexes, it holds on to the ball, supporting its weight. It walks along the surface with the ball simply rotating underneath, allowing free leg movements. While the roach's legs are in motion, the signal generated by the attached piezoelectric sensors can be monitored and analyzed. A signal conditioning system similar to that used in the experimental setup (described in the



next section) is used. It uses the same charge amplification setup, while the data is recorded through a portable oscilloscope (Tektronix, model THS720P) and transferred to a computer. Current improvement efforts are focused on replacing this data gathering setup and utilizing computer-based data acquisition equipment instead. This system is already used in the laboratory experiment setups as described in the one of the following sections.

### III.3 Laboratory setup

The experimental setup designed and built to simulate the roach testing criteria (outlined in section III.1) consists of a computer and a test bench as shown in Figure 18.

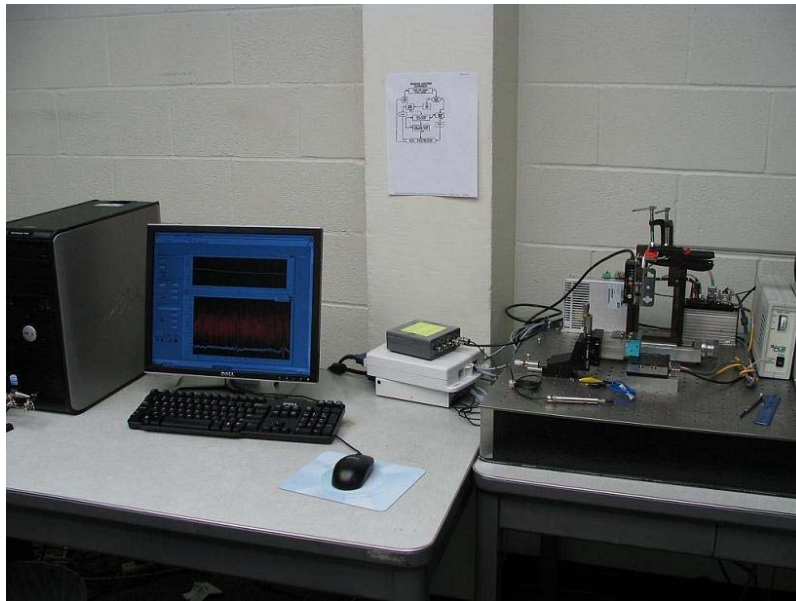


**Figure 18 Overview of experimental setup.**

The setup allows for carrying out controlled sensor deformations and gathering data feedback on sensor deflections and output signal. The results can be then analyzed to understand the behavior and performance of sensors when mounted on roaches.

### *III.3.1 Mechanical setup*

The mechanical components of the testing setup are mounted on a dampened metal breadboard (Newport, model RG-52-4). They are shown in Figure 19.

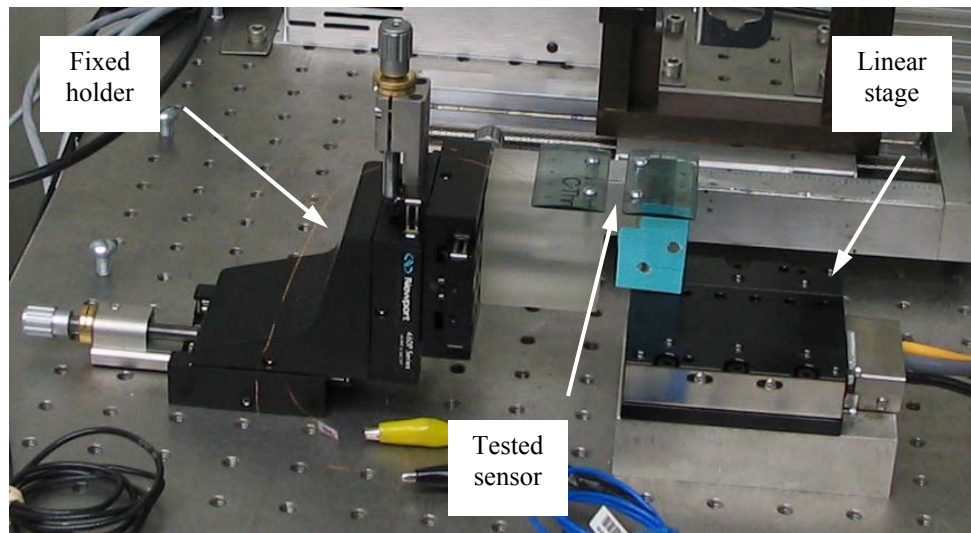


**Figure 19** Sensor mounting setup with the linear stage shown on the right.

A three-axis manual linear stage (Newport, model 460P-XYZ) shown on the left provides fixed sensor support on one end. Its adjustability in all directions allows for precise alignment of the sensor before it is tested. A single-axis miniature linear motor stage (Parker Automation, model MX80L-T02-HS-D11-H3-L2) placed on the right is responsible for generating the motion. The stage has a travel distance of 50mm with a  $5\mu\text{m}$  resolution. Both elements are fitted with custom mounting blocks used for holding the tested sensor in place as shown in Figure 20.

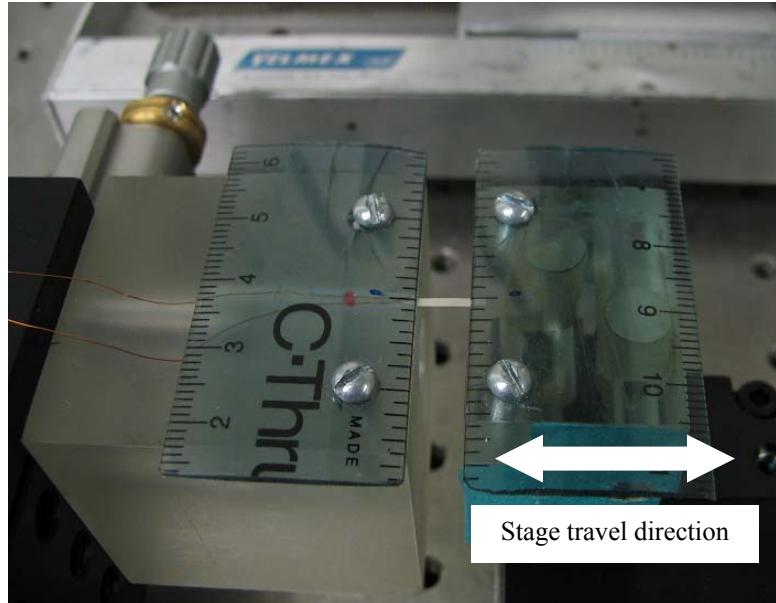


**Figure 20** Sensor mounting setup.

The sensor is fixed with the two flat mounting plates, which are tightened down with screws. Once this assembly is set up and adjusted, the sensor deflections are guided only by the travel of the linear stage. As the motorized linear stage travels left towards the fixed stand, the tested sensor buckles. Care must be taken when the stage is moving to the right, away from the fixed end. Traveling past the neutral position (when the sensor is straight, as shown in Figure 20) may result in sensor dislocation from mount or damage due to stretching. Motion is controlled and executed through the control system described in the following section.

### *III.3.2 Deflection distance gauge*

An additional part of the experimental setup is the laser deflection gauge assembly. It provides information about the shape of the buckled sensor, which can be used for verifying the buckling models discussed in a later chapter. A laser distance

gauge (Banner Engineering, model LG5A65PU), shown in Figure 21(a,b) is mounted above the PVDF sensor, such that its height can be adjusted and the laser beam is aligned vertically, pointing down at the tested PVDF sensor below.

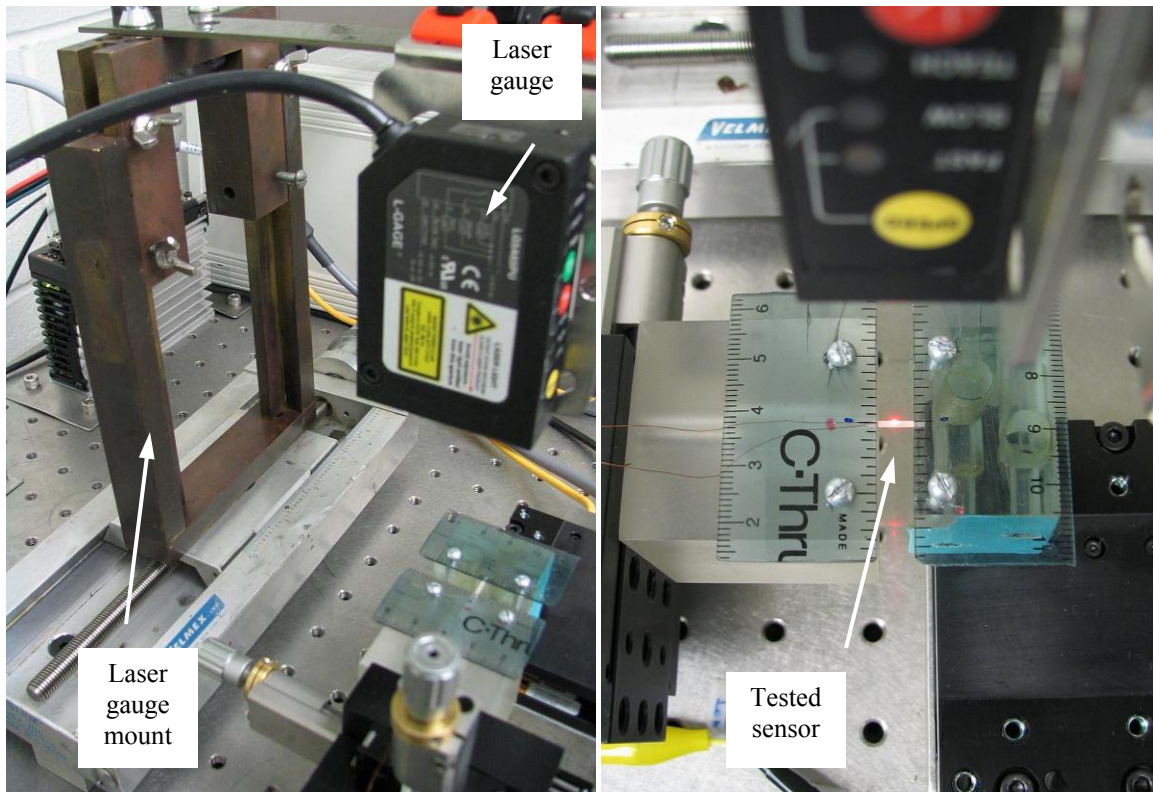


**Figure 21** Laser distance gauge setup; (a) side view, (b) angled top view.

The distance gauge has an operating range of 45-60 mm and is mounted on a linear stage, shown in Figure 21(a), allowing for movement along the length of the PVDF sensor with position measurement accuracy of 0.01" (0.254 mm). The gauge is calibrated to measure the relative change in distance to determine the sensor lateral deflection during buckling. A side view of the sensor during buckling is shown in Figure 22.

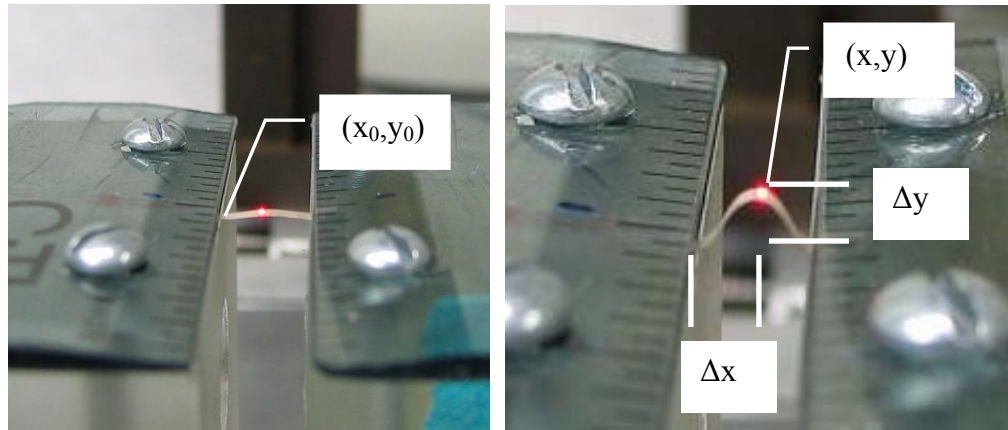


**Figure 22** Sensor lateral deflection measurement. Reference position is shown at the sensor mount.

A reference reading is taken at the stationary end of the sensor (left side), labeled as  $(x_0, y_0)$  at a point where the sensor meets the mounting block. The laser beam can then be moved horizontally through a distance  $\Delta x$  to any point along the sensor's length. The lateral deflection  $\Delta y$  can be measured at this location. The deflection shape can be thus described in terms of  $x$  and  $y$  coordinates for further use in analytical buckling modeling and charge approximation.

The gauge is powered by a power supply (Parker Automation, model XL-PSU), also shared by the linear stage and stage controller. The output from the laser gauge is wired to the input connector block (SCC-68), connected to the data acquisition board (PCI-6221). The signal is monitored by LabVIEW software, displayed in real-time on the computer screen and can be saved to a file along with other system feedback signals.

There are a number of challenges in obtaining deflection measurements while the sensor is buckled. Since one end of the sensor is fixed and the other moving, any given point along the sensor's length travels not only vertically but also in the horizontal direction as well. As a result, continuous monitoring of a single point during buckling is

very difficult. Additionally, as the sensor deflects, its surface becomes curved and the laser beam no longer strikes it at a perpendicular angle. For large sensor deflections the angle between the beam and the film surface becomes increasingly small, and it may not be possible to obtain an accurate deflection reading at every point along the sensor's length.

Given these challenges, it was decided to only use the deflection gauge in static conditions, with the sensor already buckled. By traversing the laser gauge horizontally and monitoring its position along the sensor's length, sensor deflection can be found at various points.

#### III.4 System control and data acquisition setup

In addition to controlling the linear stage movements, the control system is responsible for gathering data such as position feedback, sensor output signal and lateral deflection distance. The complete layout of the system is shown in Figure 23.

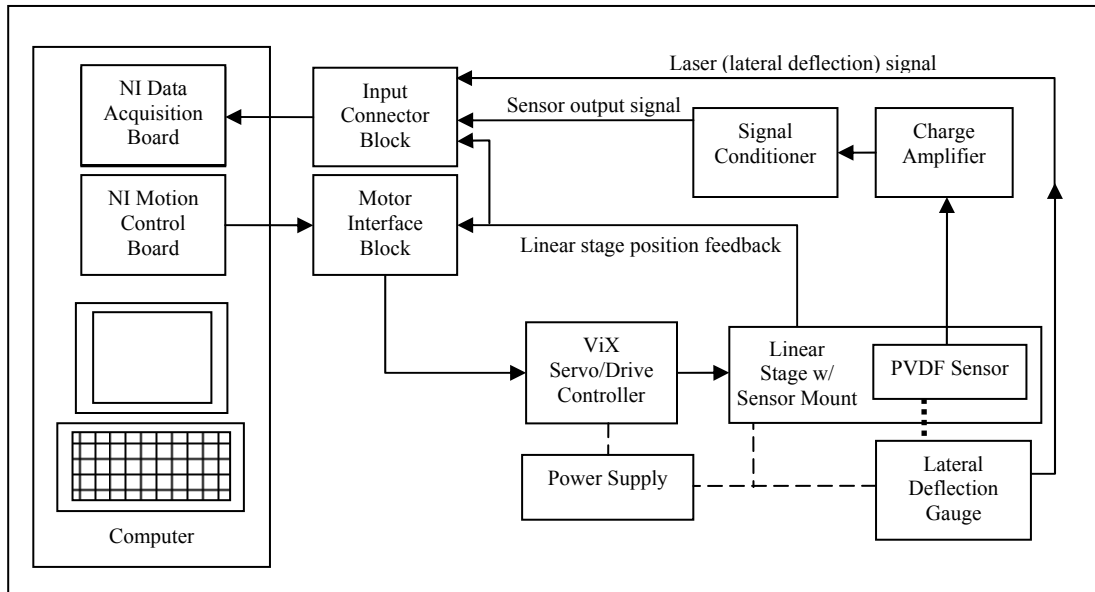


**Figure 23 Laboratory system diagram.**

System is operated by a desktop computer and controlled through a custom written programming routine in LabVIEW software (National Instruments, LabVIEW 8.0). This software setup allows for executing predefined motion paths, live system feedback monitoring, and recording data to file. The interface between the computer and the experimental setup is handled by two control boards. The motion control board (National Instruments, model PCI-7350) handles all movement commands and feedback, while the data acquisition board (National Instruments, model PCI-6221) is responsible for gathering data. Since the boards are mounted inside the computer, each one comes with an external wiring terminal, where the physical wire connections with other equipment are made. Signal inputs are connected to the input connector block (National instruments, model SCC-68), while the motion control connections are made through the motor interface block (National instruments, model UMI-7764). Specific aspects of system operations and roles of other setup elements are outlined in the next section.

### *III.4.1 Motion control*

Motion path of the motor linear stage (MX80L-T02-HS-D11-H3-L2) is defined using Microsoft Excel, and converted through the Motion Assistant software (National Instruments, Motion Assistant 2.0). It is then read through the custom control routine in LabVIEW and executed by the motion control board (PCI-7350). The control signal is sent through the universal motor interface (UMI-7764) to the linear stage controller (Parker Automation, model ViX 250AH-DRIVE). The linear stage and the controller responsible for its direct control are both powered with a DC power supply (XL-PSU).

### *III.4.2 Position feedback*

The linear stage feedback signal is transferred back to the motion control board and used by LabVIEW for real-time motion control during its operation. Feedback signal is also wired into the data acquisition board (PCI-6221) via the input connector block (SCC-68). It is then displayed on the computer screen and can be saved along with other data inputs.

### *III.4.3 Sensor signal output*

Piezoelectric sensors typically require special signal conditioning. Their output impedance is normally higher than the input impedance of most measuring devices (around several megaohms), resulting in negatively affected readings. The primary purpose of signal conditioning is to reduce the impedance of the sensor output. Several ways of achieving this goal have been studied,<sup>80,81</sup> including applications of voltage followers and current amplifiers.<sup>21</sup> Presently, charge amplifiers are most common for



measuring charge generated by the piezoelectric sensor. An example of such a device is shown in Figure 24.

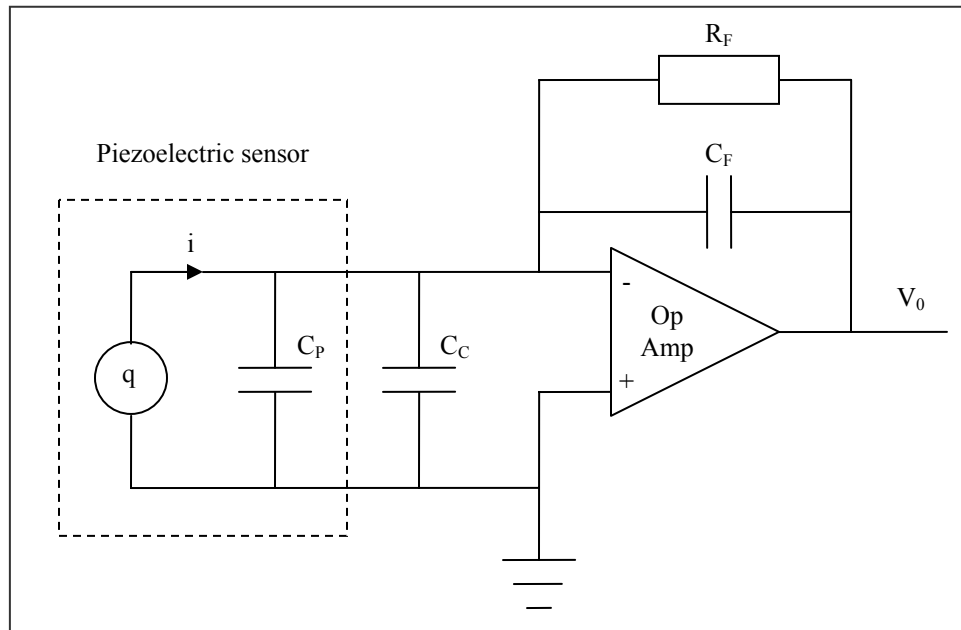


**Figure 24** Charge amplifier circuit.

The piezoelectric sensor can be modeled as a charge generator in parallel with the sensor capacitance  $C_P$  and capacitance of connecting cables  $C_C$ . The charge generated is transferred onto the feedback loop, where feedback capacitance  $C_F$  and resistance  $R_F$  can be tuned for optimal system dynamic range. By increasing the feedback capacitance, the circuit time constant is increased and the charge drain through the measurement system can be reduced, allowing for measurements at near static conditions. However, with an increased time constant the sensitivity is reduced and therefore pure static behavior cannot be measured. Another benefit of the charge amplifier is that that effect of the lead wire capacitance  $C_c$  is eliminated, therefore removing a possible source of measurement error.<sup>38,82</sup>

In this research, the PVDF sensor leads are connected to an in-line charge amplifier (PCB Piezotronics, model 422E03), where the charge output is converted to a low-impedance voltage signal (the charge conversion is 1mV/1pC). The signal then goes through an ICP® signal conditioner (PCB Piezotronics, model 482A21) where it is further refined and transferred to the data acquisition board (PCI-6221) via the input connector block (SCC-68). It is monitored by LabVIEW software, displayed in real-time on the computer screen and can be saved to file along with other system data.

#### *III.4.4 Data transfer and analysis*

As mentioned earlier, during system operation, LabVIEW software monitors and displays the system feedback information in real time. System user can save the data to file at any time. It is stored in tab-delimited format, which can be opened with most software packages. For the experiments presented here, Microsoft Excel was used for data graphing and preliminary analysis.

#### III.5 Atomic force microscopy studies

In order to further the understanding of piezoelectric behavior in the sensor, surface characterization analysis was carried out with the use of Atomic Force Microscopy (AFM). The studies were focused on determining the relationship between microstructures of PVDF and its piezoelectric behavior.

Atomic force microscopy is a technique which allows for detailed measurement of the material surface topography with a resolution as low as a few nanometers. A diagram of AFM operation is shown in Figure 25.

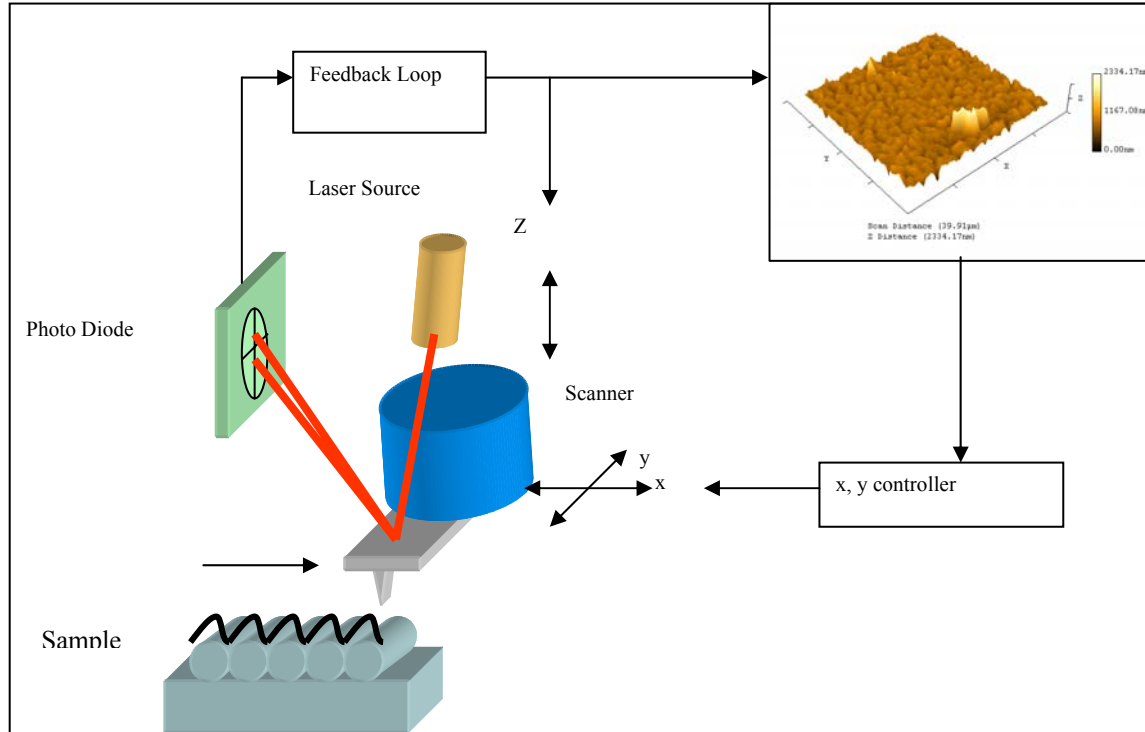


Figure 25 Schematic diagram of AFM operation.<sup>83</sup>

This technique utilizes a miniature silicone cantilever (few hundred  $\mu\text{m}$  long) with a sharp tip. It is oscillated slightly above the sample's surface and its motion becomes affected by the material underneath. Changes in oscillation amplitude are measured with a laser and a map of its surface characteristics can be created. For this study, an atomic force microscope (Pacific Nanotechnology, Nano-R™ AFM) shown in Figure 26 was used.



**Figure 26 Pacific Nanotechnology Nano-R™ atomic force microscope.<sup>84</sup>**

The AFM was operated in non-contact mode with a standard silicone probe. SPM-Cockpit (3.1.2) and Nanorule+ software was used for image processing and analysis. It is not possible to deflect or deform the PVDF film during testing, as the induced vibrations and alignment changes negatively affect AFM readings. In order to simulate the piezoelectric behavior in the PVDF, an external power supply (Sinometer, model HY3020E) was used to apply a potential to the film during the analysis. This created a charge build up and structure changes that would normally be present when the sensor is deflected. Small samples of 110  $\mu\text{m}$  NiCu-coated PVDF (Measurement Specialties, part number 3-1003702-4) were tested. The NiCu metallization layer is not as robust as the silver ink coating used for sensors, however it is thinner (60nm) and allows for more accurate measurement of the polymer underneath. The surface scan images taken with and without the applied voltage are compared and discussed further in the results chapter.

## CHAPTER IV

### RESULTS AND ANALYSIS

This section discusses the experimental data, its interpretation and comparisons with predicted results.

#### IV.1 Laboratory measurements

Initial laboratory sensor tests have provided consistent results. Figure 27 shows changes in sensor deflection and the resulting charge output as a function of time. Normalized sensor deflection, shown in yellow (light) color is a sine function with maximum amplitude of 0.4 and a frequency of 1 Hz. The charge is graphed in blue (dark).

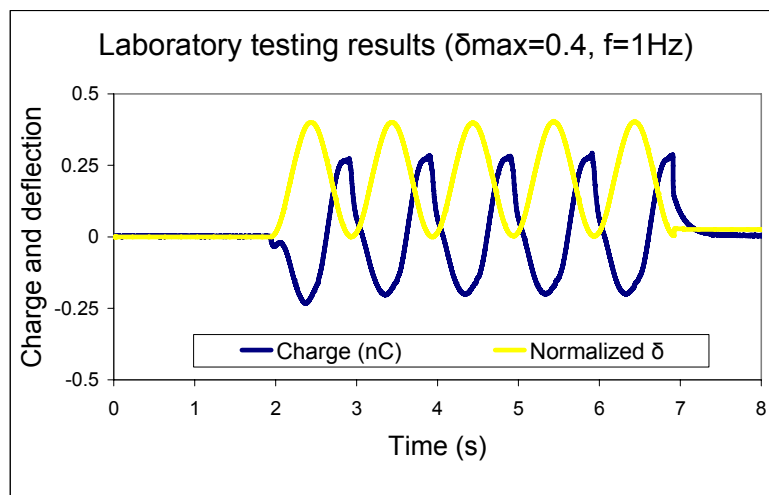


**Figure 27** Sensor charge output in relationship to buckling deflection.

The results show a consistent relationship between the two plotted values. Some distortion in the output signal shape occurs when the fully extended sensor first begins to

buckle (when  $\delta=0$ ). It is possible that these variations are introduced by the mechanical control of the experiment system. Additionally, the charge output peaks seem to be leading those of the deflection function. This will be discussed further along with the approximation results in a later section.

Additional studies were performed to determine the relationships between the sensor signal and the deflection distance and frequency. Figure 28 shows a graph of the peak sensor charge against the peak deflection amplitude.

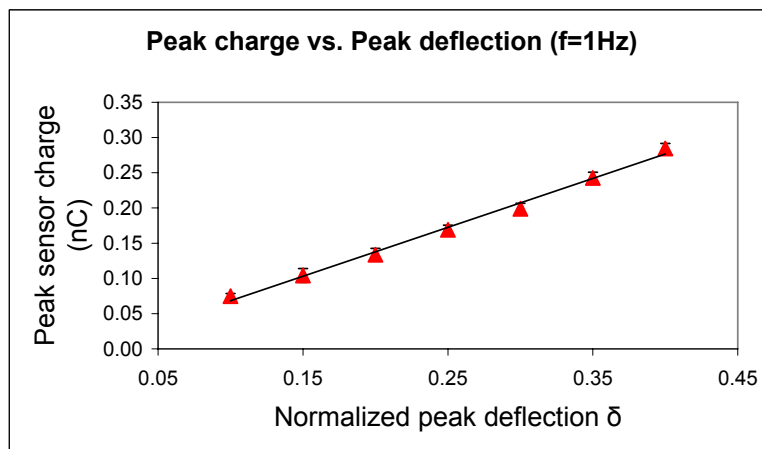


**Figure 28** Sensor piezoelectric response in relationship to buckling amplitude. (Mika et al. 2007). Reprinted with permission from SPIE.<sup>79</sup>

Normalized deflection is plotted along the horizontal axis and the peak sensor output along the vertical one. Buckling was created through a sinusoidal axial movement of the sensor's end with a fixed frequency of 1 Hz at multiple maximum deflection amplitudes. Results show that the maximum output signal is directly proportional to the maximum buckling amplitude.

Another study is focused on determining the connection between the maximum sensor output and the buckling frequency. The results are shown in Figure 29. The x-

axis is the frequency of axial deflection peaks, and the y-axis is the amplitude of the peak sensor charge. The buckling was implemented by a sinusoidal deflection function with a fixed deflection amplitude ( $\delta=0.4$ ) and at various frequencies.

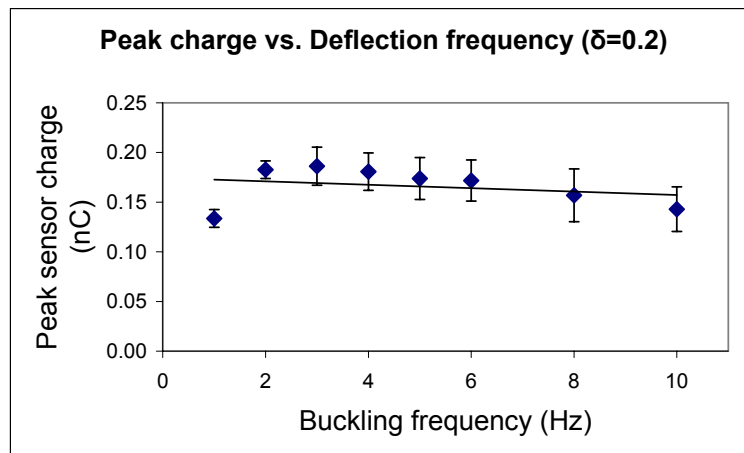


**Figure 29** Sensor piezoelectric response in relationship to buckling frequency. (Mika et al. 2007). Reprinted with permission from SPIE.<sup>79</sup>

No visible effect of the buckling frequency on the maximum output signal is observed for the frequency range tested (1-10 Hz).

The study of sensor charge relationship to deflection amplitude and frequency provides useful information about its application. Results show that charge output is directly connected to the deflection amplitude, while no relationship with the frequency is found. This suggests that individual charge signal peaks could be used to monitor the number and size of insect steps.

## IV.2 Roach experiments

Preliminary roach data was obtained by mounting a sensor across the coxa-femur joint and allowing the insect to walk along the styrofoam ball as described earlier in equipment setup section (II.4). The sensor did not seem to hinder the insects' movements and the charge generated seems fairly consistent as presented in Figure 30.

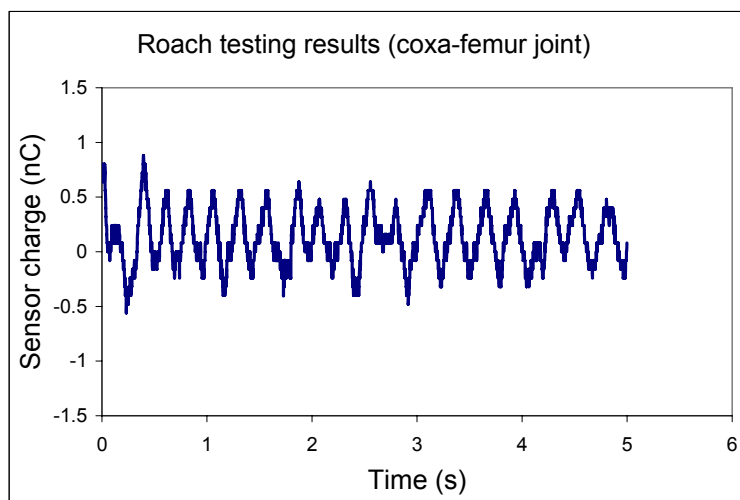


**Figure 30** Sensor charge generated due to roach movement.

The multiple charge spikes shown in the graph can be correlated with individual steps taken by the roach while walking. The shape of the output is different than the results generated by the sinusoidal deflection in the lab. For future experiments new deflection patterns can be developed (i.e. "saw-tooth" shape) to match the output results seen here. Further roach studies can be carried out to develop the recognition of insect movements and understanding of their behavior.

Larger scale experiments were initiated for this purpose. The sensor was attached to the femur-tibia joint and multiple tests were performed. Along with charge data



measurements, observations were made regarding the insect's behavior at the time. Tests were arbitrarily divided into cases when the roach was moving slowly (labeled as “walking”), or moving quickly (“running”). The recorded charge peaks were then averaged for further analysis. The results are shown in Figure 31.

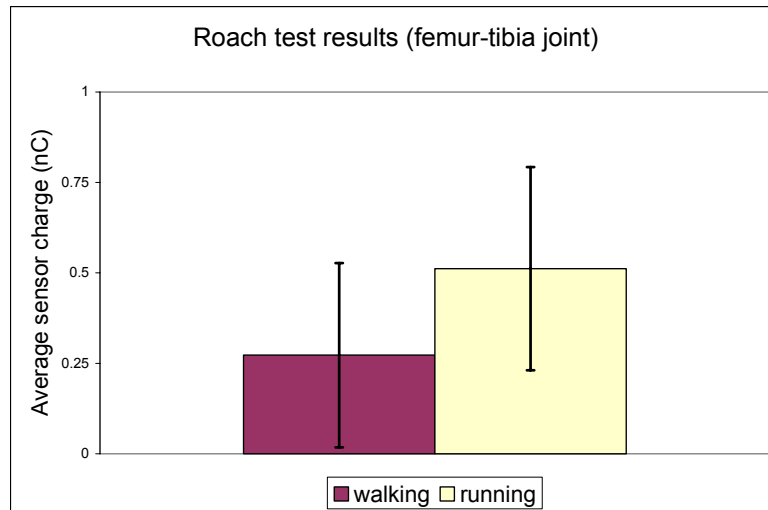


**Figure 31 Average peak charge comparisons for various insect movement speeds.**

The data indicates that on average the “running” motion developed larger charge than the “walking” movement. Given the earlier laboratory results showing the relationship between charge peaks and the deflections, it can be said that the deflection amplitudes vary depending on insect movement speed. Therefore it seems that the insect increases its movement speed by taking larger steps. Additional tests monitoring multiple legs simultaneously can be used to further the understanding of this situation, and to identify its importance in respect to overall roach behavior.

### IV.3 Analytical modeling

As mentioned earlier in the approaches section (I.10), piezoelectric films have often been studied in bending and stretching applications. No research focusing on the buckling configuration of the PVDF film has been found. This presents a unique opportunity develop and analyze a new application of this material.

#### *IV.3.1 Stress considerations*

The effectiveness of piezoelectric films in bending applications is normally improved by arranging them in multiple layers of piezo or non-piezo materials, known as unimorphs, bimorphs or multimorphs. It is also understood that single cantilever piezoelectric beams produce no signal due to bending, because the charge is cancelled by the conflicting tensile and compressive stresses.<sup>85</sup> The charge generation shown in the application presented here indicates different stress distributions between buckling and bending deflections. These differences make the buckling case an interesting topic of further analysis.

#### *IV.3.2 Existing buckling models*

Buckling behavior in has been researched extensively in the past. Because it is an inherently unstable condition, resulting solutions are often indeterminate. Detailed analyses of buckling have been used in studies of paper and fabric sheet handling applications,<sup>86,87</sup> and column deformation in vibration damping.<sup>88</sup> This research seeks to expand on this existing knowledge by implementing it into the piezoelectric analysis considerations.

### IV.3.3 Analytical models

A detailed analysis of PVDF sheet buckling has been performed for the purpose of this research and is presented in the appendix section A.1.1. A solution relating the charge output to the axial deflection  $\delta$  in buckling can be obtained through numerical approximation as:<sup>89,90</sup>

$$Q_e \approx 2d_{31}c_{11} \frac{I}{Lh} \pi^2 \left(1 + \frac{1}{2} \delta\right) (1 - \delta) \quad (4.1)$$

where the equilibrium (quasi-static) condition charge is labeled as  $Q_e$ , the piezoelectric constant is  $d_{31}$  and the elastic constant is  $c_{11}$ . Other terms include normalized axial displacement of the sensor end  $\delta$ , sensor half-length  $L$ , thickness  $h$  and cross-sectional moment of inertia  $I$ . Figure 32 shows a graph of charge output and axial deflection as a function of time.

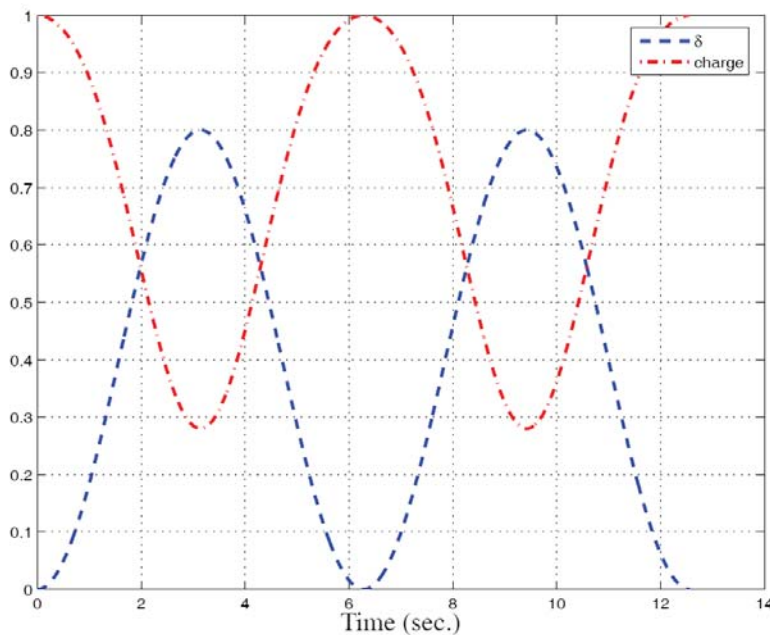


**Figure 32** Graphs of normalized sensor charge and sensor-end axial displacement  $\delta$  during buckling.<sup>90</sup>

As described in equation 4.1, and confirmed by Figure 32, the charge build up during buckling is dependent on the deflection, which is the input variable. In this case, the axial deflection of sensor's end  $\delta$  varies over time as a cosine function. Further comparisons between the estimated and experimental charge are discussed in the following chapter.

#### *IV.3.4 Lateral deflection analysis*

No detailed lateral deflection experiments have been performed so far. Their purpose is to verify the sensor deflection shape assumed for the charge modeling derivations. As explained in detail in appendix section A.1.1, the sensor shape during buckling can be defined by a sinusoidal function. It is expected that this will be confirmed by laser beam lateral deflection experiments carried out in the future phases of this project.

#### *IV.3.5 Model comparisons*

The approximate solutions obtained with the use of the sensor deflection model can be compared to the laboratory results for verification. At this time, there exist numerical discrepancies between the two sets, making a quantitative comparison between them questionable. It is still possible to use the analytical calculations for evaluating shape similarities between experimental and approximate charge graphs. Laboratory results, already presented earlier, are shown in Figure 33.

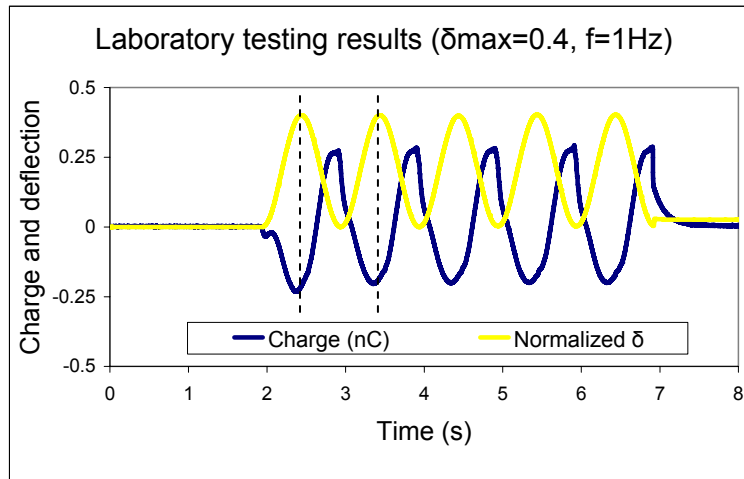


**Figure 33** Sensor output in relationship to buckling deflection – laboratory results.

The approximate analytical results scaled for the purpose of comparison are presented in Figure 34.

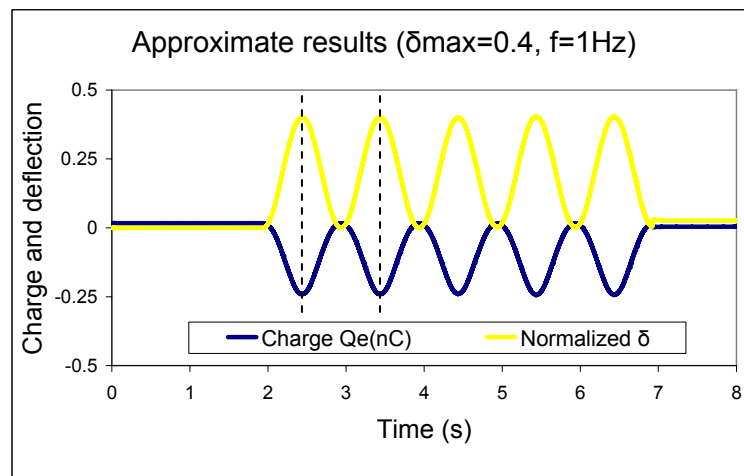


**Figure 34** Sensor output in relationship to buckling deflection – scaled analytical results.

As shown in these graphs, mathematical and experimental results provide similar sensor charge patterns during buckling. In both cases the charge becomes negative as the PVDF film is being deformed. The difference between them is that in laboratory tests,

the charge increases reaching a positive peak as the sensor returns to normal. This is not the case for the analytical results, possibly due to dynamic charge dissipation, which is not accounted for in the mathematical model. Additional discrepancies include slight output signal distortion visible in the experimental data, likely caused by the mechanical control of the linear stage, as discussed earlier. Most importantly, the laboratory charge plot seems to lead the deflection curve, which is not the case for analytical data graph. The causes of this are unknown at this time.

#### IV.4 Microscopic analysis results

Microstructure studies were performed using the AFM setup described in the experimental setup section (III.5). Results were analyzed to gain the understanding of the piezoelectric effect on the material microstructures. Figure 35 shows the AFM height (topography) image and phase (material properties) image scans taken at various testing conditions.

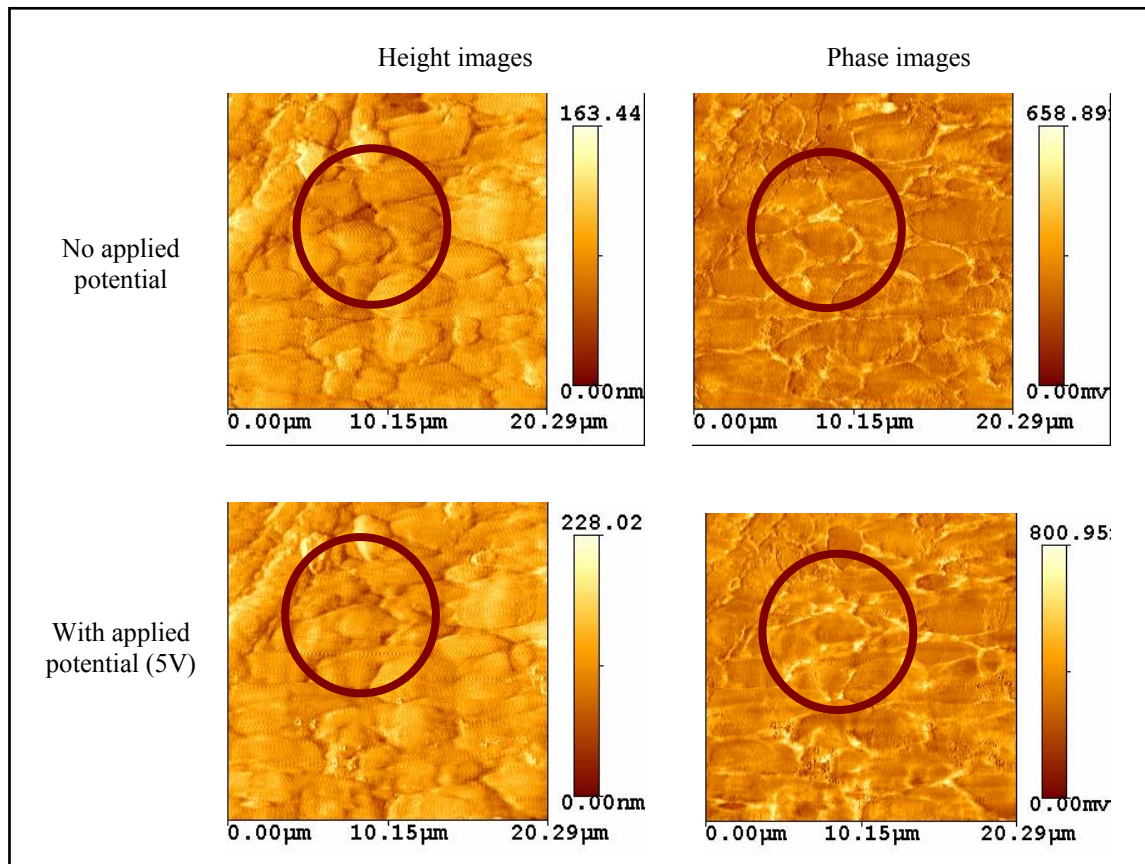


**Figure 35** AFM height and phase images of the PVDF material. (Mika et al. 2007). Reprinted with permission from SPIE.<sup>79</sup>

The material grains visible in the height images are on the order of a few micrometers in size, separated by clear boundaries with individual material voids (highlighted with a circle). When a 5V electrical potential is applied, the spaces between grains seem to become smaller, the voids reduced in size and the sample more uniform in height. Additionally, an increase in surface height is noted. Similar results are confirmed by the phase images. Further analysis is performed using line scans of the surface features. Two directions of scans are studied: vertical and horizontal. Figure 36 shows the measurements taken with no voltage applied.

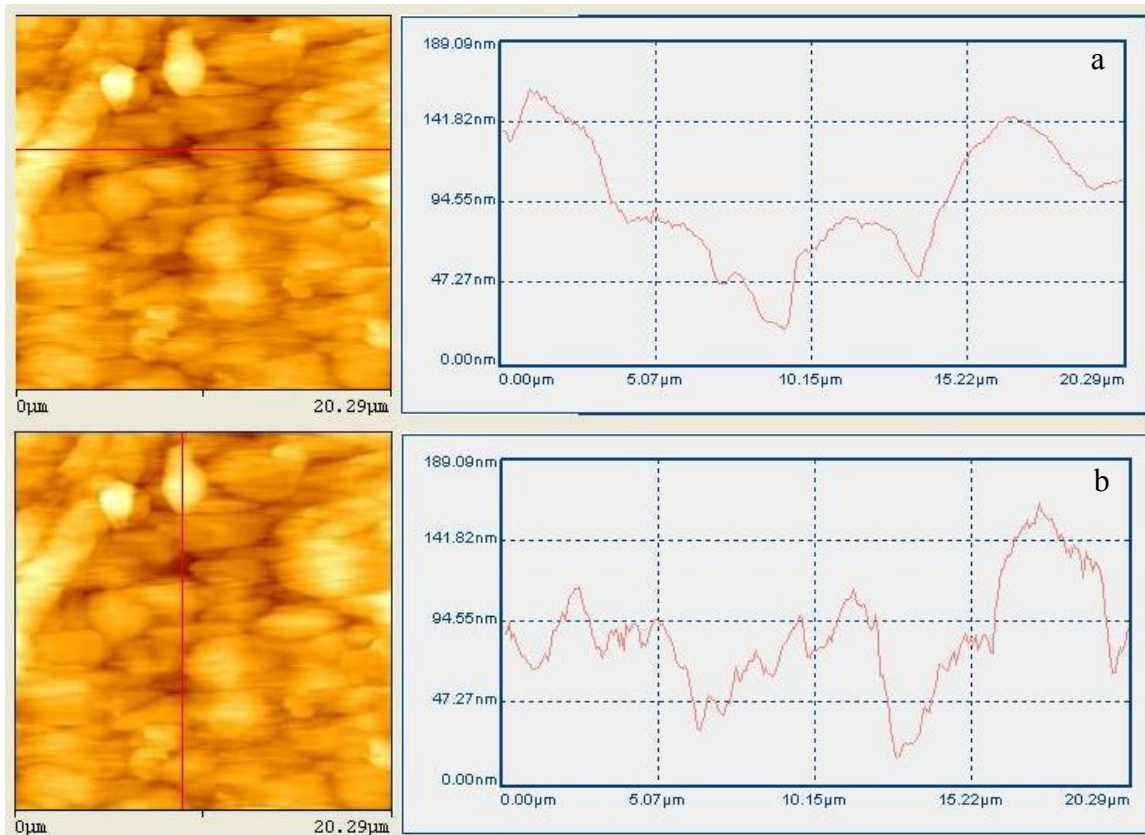


**Figure 36 AFM Line scans with no applied potential: (a) horizontal, (b) vertical.**

Figure 37 shows the readings taken over the same area with an applied potential of 5V.



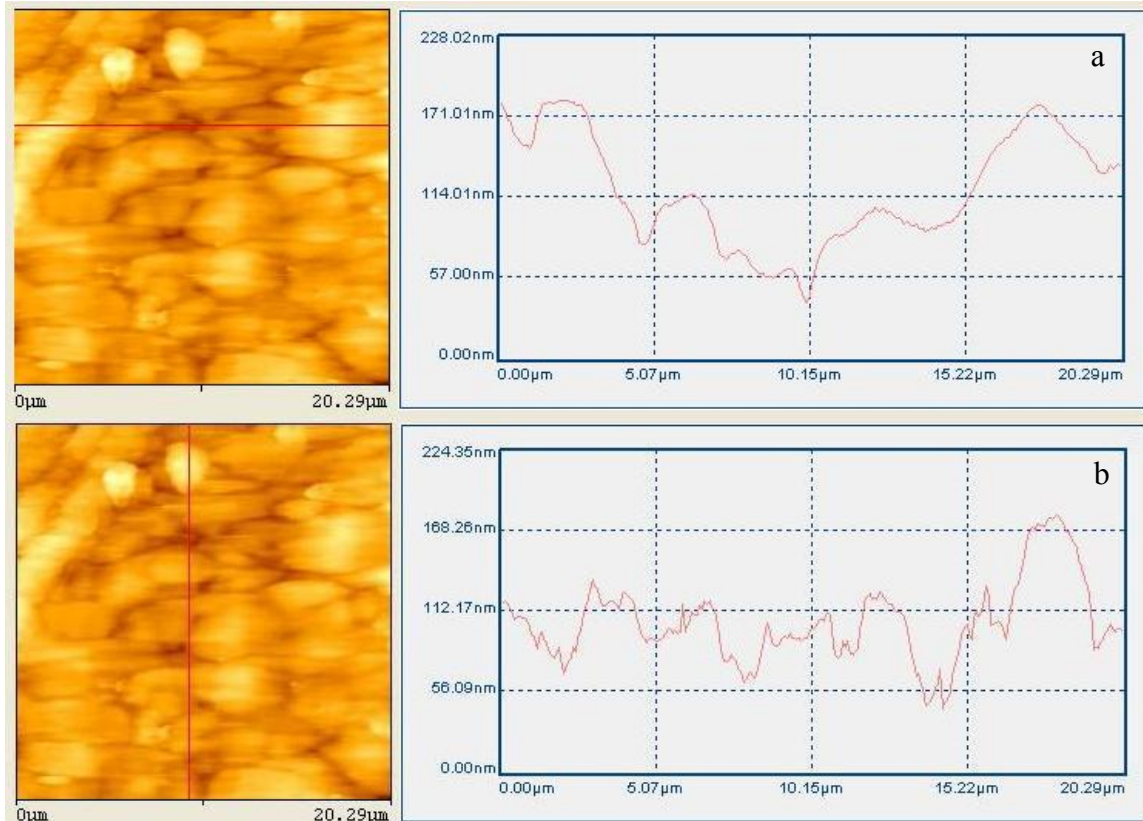


**Figure 37 Line scans with 5V applied potential: (a) horizontal, (b) vertical**

The results were reviewed to determine the changes occurring due to the applied voltage. Data comparisons are shown in Table 2.

**Table 2 PVDF sample AFM line scans - surface height comparisons.**

	PVDF surface height (nm)		
	Maximum	Minimum	Range
No applied potential			
Horizontal scan	155	25	130
Vertical scan	165	30	135
5V applied potential			
Horizontal scan	185	40	140
Vertical scan	175	45	130

The results do not confirm the suspected changes in material grains. It is possible that these perceived changes of surface structures are due the differences in height scales of the images in Figure 35. Instead, the line scans show an overall increase of surface height with applied voltage. This is likely an example of an inverse of the piezoelectric effect discussed earlier (section I.6), where as shown in Equation 1.16, the charge build up in the film is related to the change of its thickness.

This behavior is likely due to the dipole changes inside the piezomaterial. Under an applied potential, the dipole alignment affects the material properties, leading to changes in thickness. Detailed mechanisms of surface microstructure changes within PVDF are an interesting research topic and have been studied in the past.<sup>79,91,92</sup> Performing in-situ microscopy studies on the piezoelectric effects remains a new and exciting area of research and future developments can be expected.

## CHAPTER V

### CONCLUSIONS

This project has been an important step in developing a new research area. It has achieved three main goals:

- developed a methodology and hardware for sensor testing,
- completed initial sensor testing and analysis,
- proved feasibility of insect studies with piezoelectric sensors.

Specifically, two test systems have been designed and built. One for analyzing the piezoelectric response in PVDF films due to buckling, and another for sensor application studies on the roach, *Blaberus discoidalis*. An understanding of piezoelectric materials has been achieved through study of existing literature and analysis of new laboratory experiments. A new sensor application was shown to be a promising tool for future studies of insects, their movements and behaviors. Also, initial steps were taken in the area of surface microstructure studies of PVDF and their relationship with the piezoelectric effect.

A knowledge base of materials, sensors, equipment setups and basic insect behavior has been established and documented for use in the next phases of the project. Given the early stage of this research, a number of future improvements can be made. The following topics have been identified as possible areas of future developments:

- improved sensor manufacturing processes (die cutting techniques, conductive adhesives, protective coatings - i.e. parylene),
- new sensor-to-roach attachment methods (glues or clamps),

- extensive roach testing (multiple-leg testing in combination with behavioral monitoring to facilitate the identification and understanding of insect movement patterns and their connection with piezo sensor response).

The application of the above suggestions will likely further increase the reliability and usefulness of thin film PVDF sensors as tools for physiological studies of insects.

## REFERENCES

- <sup>1</sup> J. Curie and P. Curie, C. R. Acad. Sci. Paris **91**, 294, (1880); **91**, 383 (1880).
- <sup>2</sup> L. Kelvin, *Baltimore Lectures* (C.J. Clay & Sons, London, 1904).
- <sup>3</sup> P. Langevin, French Patent No. 505 (17 September 1918), p. 703.
- <sup>4</sup> W. G. Cady, *Piezoelectricity* (McGraw Hill, New York, 1946; Dover, New York, 1964).
- <sup>5</sup> H. Kawai, Japan J. Appl. Phys. **8**, 975 (1969).
- <sup>6</sup> M. G. Broadhurst, G. T. Davis, in *Electrets* edited by G. M. Sessler (Springer-Verlag, Berlin, vol. 33, 1980), pp. 285-319.
- <sup>7</sup> M. G. Broadhurst, G. T. Davis, J. E. McKinney, and R. E. Collins, J. Appl. Phys. **49**, 4992 (1978).
- <sup>8</sup> G. M. Sessler, J. Acoust. Soc. Am. **70**, 1596 (1981).
- <sup>9</sup> R. Hasegawa, Y. Takahashi, Y. Chatani, and H. Tadokoro, Polym. J. **3**, 600 (1972).
- <sup>10</sup> M. A. Bachmann and J. B. Lando, Macromolecules **14**, 40 (1981).
- <sup>11</sup> S. Weinhold, M. H. Litt, and J. B. Lando, Macromolecules **13**, 1178 (1980).
- <sup>12</sup> A. J. Lovinger, Macromolecules **14**, 322 (1981).
- <sup>13</sup> A. J. Lovinger, Macromolecules **15**, 40 (1982).
- <sup>14</sup> G. T. Davis, J. E. McKinney, M. G. Broadhurst, and S. C. Roth, J. Appl. Phys. **49**, 4998 (1978).
- <sup>15</sup> A. J. Lovinger, Science **220**, 1115 (1983).
- <sup>16</sup> H. D. Keith and F. J. Padden, Jr., J. Appl. Phys. **35**, 1270 (1964).
- <sup>17</sup> A. J. Lovinger, Polymer **21**, 1317 (1980).
- <sup>18</sup> A. J. Lovinger, J. Appl. Phys. **52**, 5934 (1981).
- <sup>19</sup> K. Nakagawa and Y. Ishida, J. Polym. Sci. Phys. Ed. **11**, 2153 (1973).
- <sup>20</sup> B. L. Farmer, A. J. Hopfinger, and J. B. Lando, J. Appl. Phys. **43**, 4293 (1972).

- <sup>21</sup> C. K. Lee and T. C. O'Sullivan, *J. Acoust. Soc. Am.* **90**, 949 (1991).
- <sup>22</sup> R. M. Bozorth, *Ferromagnetism* (Van Nostrand, New York, 1951; IEEE Press, Piscataway, 1993).
- <sup>23</sup> J. S. Harrison and Z. Ounaies, NASA/CR-2001-211422, ICASE Report No. 2001-43 (2001).
- <sup>24</sup> H. Sussner and K. Dransfeld, *J. Polym. Sci. Polym. Phys. Ed.* **16**, 529 (1978).
- <sup>25</sup> R. G. Kepler and R. A. Anderson, *J. Appl. Phys.* **49**, 1232 (1978).
- <sup>26</sup> J. P. Luongo, *J. Polym. Sci. A-2* **10**, 1119 (1972).
- <sup>27</sup> K. Tashiro, M. Kobayashi, H. Tadakoro, and E. Fukada, *Macromolecules* **13**, 691 (1980).
- <sup>28</sup> T. Furukawa, *IEEE Trans. Electr. Insul.* **24**, 375 (1989).
- <sup>29</sup> G. M. Sessler, D. K. Das-Gupta, A. S. DeReggi, W. Eisenmenger, T. Furukawa, J. A. Giacometti, and R. Gerhard-Multhaupt, *IEEE Trans. Electr. Insul.* **27**, 872 (1992).
- <sup>30</sup> E. P. Adams, *J. Franklin Inst.* **204**, 469 (1927).
- <sup>31</sup> F. I. Mopsik and M. G. Broadhurst, *J. Appl. Phys.* **46**, 4204 (1975).
- <sup>32</sup> H. Ohigashi, *J. App. Phys.* **47**, 949 (1976).
- <sup>33</sup> R. Hayakawa and Y. Wada, *Rep. Progr. Polym. Phys. Jpn.* **19**, 321 (1976).
- <sup>34</sup> Y. Wada and R. Hayakawa, *Ferroelectrics* **32**, 115 (1981).
- <sup>35</sup> A. Ballato, *IEEE Trans. Ultrason., Ferroelect., Freq. Control* **42**, 916 (1995).
- <sup>36</sup> W. P. Mason, *Physical Acoustics and the Properties of Solids* (Van Nostrand, Princeton, 1958).
- <sup>37</sup> A. H. Meitzler, H. F. Tiersten, A. W. Warner, D. Berlincourt, G. A. Coquin, and F. S. Welsh III, *IEEE Standard on Piezoelectricity* (IEEE, New York, 1988).
- <sup>38</sup> J. Sirohi, I. Chopra, *J. Intellig. Mat. Sys. Struct.* **11**, 246 (2000).
- <sup>39</sup> E. Fukada and T. Furukawa, *Ultrasonics* **1**, 31 (1981).
- <sup>40</sup> T. Yamada, *J. Appl. Phys.* **53**, 6335 (1982).

- <sup>41</sup> V. V. Kochervinskii, *Russ. Chem. Rev.* **65**, 865 (1996).
- <sup>42</sup> T. Furukawa and T. T. Wang, in *The Applications of Ferroelectric Polymers* edited by T. T. Wang, J. M. Herbert, and A. M. Glass (Blackie, U.K., 1987), pp. 66-117.
- <sup>43</sup> K. Tashiro, H. Tadakoro, and M. Kobayashi, *Ferroelectrics* **32**, 167 (1981).
- <sup>44</sup> H. J. Shaw, D. Weinstein, L. T. Zitelli, C. W. Frank, R. C. DeMattei, and K. Fesler, *Proc. 1980 Ultrason. Symp.* (IEEE, Piscataway, 1980), pp. 927-940.
- <sup>45</sup> E. L. Nix, L. Holt, J. C. McGrath, and I. M. Ward, *Ferroelectrics* **32**, 103 (1981).
- <sup>46</sup> E. Fukada and T. Sakurai, *Polym. J.* **2**, 656 (1971).
- <sup>47</sup> G. Gerliczy and R. Betz, *Sensors and Actuators* **12**, 207 (1987).
- <sup>48</sup> J. McKinney, G. T. Davis, and M. G. Broadhurst, *J. Appl. Phys.* **51**, 1676 (1980).
- <sup>49</sup> P. D. Southgate, *Appl. Phys. Lett.* **28**, 250 (1976).
- <sup>50</sup> Arkema, Inc., [http://www.arkema-inc.com/literature\\_techpoly.cfm?pag=102](http://www.arkema-inc.com/literature_techpoly.cfm?pag=102);  
<http://www.arkema-inc.com/index.cfm?pag=102>, Accessed May 2007.
- <sup>51</sup> G. Eberle, H. Schmidt, and W. Eisenmenger, *IEEE Trans. Dielectrics Electr. Insul.* **3**, 624 (1996).
- <sup>52</sup> Y. Bar-Cohen, *Electroactive Polymer (EAP) Actuators as Artificial Muscles: Reality, Potential and Challenges* (SPIE, Bellingham, 2001), p. 615.
- <sup>53</sup> D. De Rossi and P. Dario, *Medical Applications of Piezoelectric Polymers* edited by P. M. Galletti, D. E. De Rossi, and A. S. De Reggi (Gordon and Breach, New York, 1988), p. 83.
- <sup>54</sup> Measurement Specialties, <http://www.meas-spec.com/myMeas/download/pdf/english/piezo/techman.pdf>, Accessed May 2007.
- <sup>55</sup> D. Fox, *Ferroelectrics* **115**, 215 (1991).
- <sup>56</sup> A. M. Vinogradov, S. C. Schumacher, and E. M. Rassi, *J. Appl. Electromag. Mech.* **22**, 39 (2005).
- <sup>57</sup> Y. Gu, R. L. Clark, C. R. Fuller, and A. C. Zander, *J. Vibration and Acoustics* **116**, 303 (1994).
- <sup>58</sup> H. S. Tzou, *J. Robotic Systems* **6**, 745 (1989).

- <sup>59</sup> F. Delcomyn, *J. Exp. Biol.* **54**, 443 (1971).
- <sup>60</sup> F. Delcomyn, *J. Exp. Biol.* **133**, 111 (1977).
- <sup>61</sup> N. J. Cowan, J. Lee, and R. J. Full, *J. Exp. Biol.* **209**, 1617 (2006).
- <sup>62</sup> J. T. Watson and R. E. Ritzmann, *J. Comp. Physiol.* **182**, 11 (1998).
- <sup>63</sup> J. T. Watson and R. E. Ritzmann, *J. Comp. Physiol.* **182**, 23 (1998).
- <sup>64</sup> J. T. Watson, R. E. Ritzmann, and A. J. Pollack, *J. Comp. Physiol.* **188**, 55 (2002).
- <sup>65</sup> D. R. Reynolds and J. R. Riley, *Comput. Electron. Agr.* **35**, 271 (2002).
- <sup>66</sup> W. Kutsch, *Theory in Biosciences* **118**, 29 (1999).
- <sup>67</sup> I. G. Priede and S. M. Swift, *Ecology* **74**, 1908 (1993).
- <sup>68</sup> T. G. Wolcott, *J. Exp. Mar. Biol. Ecol.* **193**, 257 (1995).
- <sup>69</sup> F. G. Barth and P. Pickelmann, *J. Comp. Physiol.* **103**, 39 (1975).
- <sup>70</sup> A. Skordos, P. H. Chan, J. F. V. Vincent, and G. Jeronimidis, *Phil. Trans. R. Soc. Lond. A* **360**, 239 (2002).
- <sup>71</sup> University of Massachusetts, <http://www.bio.umass.edu/biology/kunkel/cockroach.html>, Accessed May 2007.
- <sup>72</sup> B. E. Hagenbuch, P. G. Koehler, R. S. Patterson, and R. J. Brenner, *J. Med. Entomol.* **25**, 377 (1988).
- <sup>73</sup> W. J. Bell and K. G. Adiyodi, *The American Cockroach* (Chapman and Hall, London, 1981).
- <sup>74</sup> M. K. Rust, D. A. Reiersen, and K. H. Hansgen, *J. Med. Entomol.* **28**, 210 (1991).
- <sup>75</sup> Measurement Specialties, [http://www.meas-spec.com/myMeas/MEAS\\_download/Catalogs/Piezo/catalog\\_price\\_list.pdf](http://www.meas-spec.com/myMeas/MEAS_download/Catalogs/Piezo/catalog_price_list.pdf), Accessed May 2007.
- <sup>76</sup> Y. Fu, E. C. Harvey, M. K. Ghantasala, and G. M. Spinks, *Smart Mater. Struct.* **15**, S141-S146 (2006).
- <sup>77</sup> Courtesy of H. Lee, Dept. of Mat. Sci. Engr., Texas A&M University.
- <sup>78</sup> R. J. Full and M. S. Tu, *J. Exp. Biol.* **148**, 129 (1990).



- <sup>79</sup> B. Mika, H. Lee, J. M. Gonzalez, S. B. Vinson, and H. Liang, Proc. of SPIE **6528**, 652817 (2007).
- <sup>80</sup> D. F. Stout and M. Kaufman, *Handbook of Operational Amplifier Circuit Design* (McGraw Hill, New York, 1976).
- <sup>81</sup> J. W. Dally, W. F. Riley, and K. G. McConnell, *Instrumentation for Engineering Measurement*. (John Wiley & Sons, New York, 1993).
- <sup>82</sup> P. Horowitz and W. Hill, *The Art of Electronics* (Cambridge U. P., Cambridge, England, 1980).
- <sup>83</sup> T. Jee, MS Thesis, Dept. of Mech. Engr., Texas A&M University, 2005.
- <sup>84</sup> Pacific Nanotechnology, <http://www.pacificnanotech.com/nano-r-afm.html>, Accessed May 2007.
- <sup>85</sup> Q. M. Wang, X. Du, B. Xu, and L. E. Cross, J. Appl. Phys. **85**, 1702 (1999).
- <sup>86</sup> C. Y. Wang, ASME J. Appl. Mech. **51**, 278 (1984).
- <sup>87</sup> S. T. Santillan, L. N. Virgin, and R. H. Plaut, ASME J. Appl. Mech. **73**, 664 (2006).
- <sup>88</sup> H. S. Yoon, G. Washington, and A. Danak, J. Intellig. Mat. Sys. Struct., **16**, 877 (2005).
- <sup>89</sup> K. S. Moon, H. Liang, J. Yi, and B. Mika, Proc. of SPIE **6529**, 65290 (2007).
- <sup>90</sup> J. Yi, Dept of Mech. Engr., San Diego State University (unpublished manuscript), (2007).
- <sup>91</sup> T. Jee, H. Lee, B. Mika, and H. Liang, Tri. Lett. **26**, 125 (2007).
- <sup>92</sup> S. Mani, R. Perez, H. Lee, Z. Ounaies, W. Hung, and H. Liang, J. Trib., in press (2007).

## APPENDIX A

### EQUATIONS AND DERIVATIONS

#### A.1 Approximate charge generation during buckling

Following is a derivation of the approximate charge resulting due to sensor buckling deformation based on the work of Yi<sup>90</sup> and other authors referenced within.\*

##### *A.1.1 Analytical derivation*

We denote the PVDF elastica size as  $2L$  (length),  $b$  (width), and  $h$  (height), respectively. Since the PVDF film is very thin (around 110  $\mu\text{m}$ ), we can consider this sensor as a thin strip and use the heavy elastica model discussed by Wang<sup>86</sup> and Santillan et al.<sup>87</sup> to model the deflection of the post-buckling shape of the sensor. We consider a PVDF based elastica that is under buckling formation as shown in Figure A1(a). One end of the PVDF elastica is clamped at a fixed platform and the other end is also clamped with a moving platform. The deformation of the moving end is denoted as  $\Delta(t)$  and the applied force is denoted as  $F(t)$ .

---

\* Reprinted with permission from:

“On Symmetric Buckling of a Finite Flat-Lying Heavy Sheet” by C.Y. Wang, 1984. *ASME Journal of Applied Mechanics*, Vol. 51, p.278–282, Copyright ©1984 by ASME. and

“Post-Buckling and Vibration of Heavy Beam on Horizontal or Inclined Rigid Foundation” by S. T. Santillan, L. N. Virgin, and R. H. Plaut, 2006. *ASME Journal of Applied Mechanics*, Vol. 73, p.664–671, Copyright ©2006 by ASME.

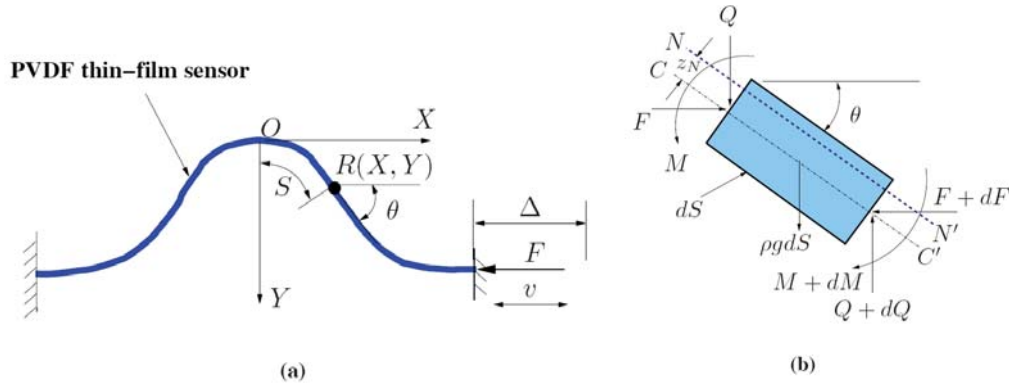


**Figure A1 : (a) Schematic of the buckling shape of a PVDF sensor; (b) free body diagram of a differential element of the sensor.**

We choose the  $XY$  coordinate with origin  $O$  at the fixed end of the PVDF sensor. The deflection at point  $R(X, Y)$  of the PVDF strip is parameterized by the arc-length  $S$  (with  $S=0$  at point  $O$ ) as shown in Figure A1 (a). The deflection angle  $\theta(S)$  is defined as the tangent directional angle with the  $X$  axis. Figure A1 (b) shows the free body diagram of at point  $R$ . The internal forces along  $X$  and  $Y$  directions on the differential element  $dS$  at time  $T$  are denoted as  $F(S, T)$  and  $Q(S, T)$ , respectively. The bending moment at point  $R$  is denoted as  $M(S, T)$  at time  $T$ . We can then obtain the motion equation for the elastica as:<sup>†</sup>

$$\begin{aligned} \frac{\partial X}{\partial S} &= \cos \theta, & \frac{\partial Y}{\partial S} &= \sin \theta, & \frac{\partial \theta}{\partial S} &= \kappa = \frac{M}{EI}, \\ \frac{\partial F}{\partial S} &= -\rho \frac{\partial^2 X}{\partial T^2}, & \frac{\partial Q}{\partial S} &= -\rho g - \rho \frac{\partial^2 Y}{\partial T^2}, & \frac{\partial M}{\partial S} &= Q \cos \theta - F \sin \theta, \end{aligned} \quad (\text{A1.1})$$

where  $E$  is Young's modulus of the PVDF film,  $I$  is the second moment of the cross sectional area of the elastica with respect to the bending axis, and  $\rho$  is the mass density per unit length of the PVDF material. Before we proceed to put Eq. (A1.1) into

---

<sup>†</sup> For notation simplicity, we drop the variable dependence on arc length  $S$  and time  $T$ .

dimensionless equations, we first determine the electric charge  $Q_e$ . We consider the linear constitutive relationships<sup>37</sup> for piezoelectricity among strain ( $S$ ), stress ( $T$ ), electric field ( $E$ ), and electric displacement ( $D$ )

$$\begin{aligned} S_j &= s_{ji}^E T_i + d_{jm} \varepsilon_m \\ D_m &= d_{mj} T_j + \varepsilon_{km}^E \varepsilon_k \end{aligned} \quad (\text{A1.2})$$

where  $s$  is the compliance matrix,  $d$  is the piezoelectric matrix, and  $\varepsilon$  is the permittivity matrix. Moreover, we assume that the electric field is approximately close to zero due to the quasi-static estimation in this study. The accumulated electric charge  $Q_e$  due to the bending and axial forces on the two sides of the PVDF sensor electrodes can be calculated as:<sup>88</sup>

$$Q_e = \int_A D_3 dA = d_{31} c_{11} \int_A S_1 dA \quad (\text{A1.3})$$

where  $D_3$  is electric displacement along 33 direction and  $dA$  is the electrode area of the strip surface. Since the PVDF film is not stiff, we consider the electric charge is mainly generated by the bending of the PVDF film. For the differential PVDF element shown in Figure A1(b), the element is under both bending and axial force and the neutral axis ( $NN'$  in Figure A1(b)) of the PVDF film will no longer be the film centroidal axis ( $CC'$  in Figure A1(b)). Denote the distance between  $NN'$  and  $CC'$  as  $z_N$  at location  $S$  and time  $T$ . Then the axial force  $F_a$  along the sensor film is given by:

$$F_a = F \cos \theta + Q \sin \theta \quad (\text{A1.4})$$

and the bending moment is  $M$ . Note that the strain  $S = \theta$  along  $NN'$  and using the superposition of axial force and bending moment effects, we can calculate  $z_N$  as:

$$z_N = \frac{1}{12} \frac{F_a}{M} h^2 = \frac{1}{12} \frac{F \cos \theta + Q \sin \theta}{M} h^2 \quad (\text{A1.5})$$

Then the strain  $S_1$  of the single PVDF film can be calculated as:

$$S_1 = z_N \kappa = \frac{1}{12} \frac{F \cos \theta + Q \sin \theta}{M} h^2 \frac{M}{EI} = \frac{F \cos \theta + Q \sin \theta}{Ebh} \quad (\text{A1.6})$$

where we use  $I = \frac{1}{12} bh^3$  for a rectangular cross section area. Due to the

symmetry of the film we only consider  $S > 0$  and thus write Eq. (A1.3) as:

$$Q_e = 2bd_{31}c_{11} \int_0^L z_N \kappa dS = \frac{d_{31}c_{11}}{Eh} \int_0^L (F \cos \theta + Q \sin \theta) dS \quad (\text{A1.7})$$

We can use the following non-dimensional quantities<sup>87</sup> for dynamic equations of motion given by Eq. (A1.1):

$$\begin{aligned} x &= \frac{X}{L}, \quad y = \frac{Y}{L}, \quad s = \frac{S}{L}, \quad \delta = \frac{\Delta}{L}, \quad m = \frac{ML}{EI}, \quad f = \frac{FL^2}{EI}, \\ q &= \frac{QL^2}{EI}, \quad w = \frac{\rho g L^3}{EI}, \quad t = \frac{T}{L^2} \sqrt{\frac{EI}{\rho}}, \quad \Omega = wL^2 \sqrt{\frac{\rho}{EI}} \end{aligned} \quad (\text{A1.8})$$

and Eq. (A1.1) becomes:

$$\begin{aligned} \frac{\partial x}{\partial s} &= \cos \theta, \quad \frac{\partial y}{\partial s} = \sin \theta, \quad \frac{\partial \theta}{\partial s} = m, \\ \frac{\partial f}{\partial s} &= -\frac{\partial^2 x}{\partial t^2}, \quad \frac{\partial q}{\partial s} = -w - \frac{\partial^2 y}{\partial t^2}, \quad \frac{\partial m}{\partial s} = q \cos \theta - f \sin \theta, \end{aligned} \quad (\text{A1.9})$$

Furthermore, we can separate the variables as the sum of equilibrium and dynamic components, namely:

$$\begin{aligned} x(s,t) &= x_e(s) + x_d(s) \sin(\Omega t), \quad y(s,t) = y_e(s) + y_d(s) \sin(\Omega t), \\ \theta(s,t) &= \theta_e(s) + \theta_d(s) \sin(\Omega t), \quad m(s,t) = m_e(s) + m_d(s) \sin(\Omega t), \\ f(s,t) &= f_e(s) + f_d(s) \sin(\Omega t), \quad q(s,t) = q_e(s) + q_d(s) \sin(\Omega t), \end{aligned} \quad (\text{A1.10})$$

Then we can write the equations that the equilibrium components must satisfy as:

$$\frac{\partial x_e}{\partial s} = \cos \theta_e, \quad \frac{\partial y_e}{\partial s} = \sin \theta_e, \quad \frac{\partial \theta_e}{\partial s} = m_e, \quad \frac{\partial m_e}{\partial s} = q_e \cos \theta_e - f_e \sin \theta_e, \quad (\text{A1.11})$$

The normalized force  $q_e$  satisfies:

$$q_e(s) = sw \quad (\text{A1.12})$$

since  $q_e$  is the normalized gravity force from  $S=0$ . The boundary conditions for Eq. (A1.11) are:

$$x_e(0) = y_e(0) = \theta_e(0) = 0, \quad x_e(1) = 1 - \delta, \quad \theta_e(1) = 0 \quad (\text{A1.13})$$

For the electric charge generated by the buckling, we only consider the charge generated by the quasi-static equilibria and therefore we can write Eq. (A1.7) as:

$$Q_e = 2bd_{31}c_{11} \frac{I}{Lh} \int_0^1 (f_e \cos \theta_e + q_e \sin \theta_e) ds \quad (\text{A1.14})$$

### A.1.2 Approximate solution

The exact analytical solutions for differential equations given by Eq. (A1.11) with boundary conditions (A1.13) cannot be obtained.<sup>86</sup> Therefore, we approximate the boundary value problem following the same approach taken by Wang.<sup>86</sup> For small deflections  $\theta \ll 1$  for the PVDF film, we can assume that  $w \ll 1$ . We assume  $w = \varepsilon^3 \ll 1$  and we can approximate  $\theta e(s)$ ,  $x e(s)$ ,  $y e(s)$  and  $f e(s)$  as:

$$\begin{aligned} \theta_e(s) &= \varepsilon \theta_0(s) + \varepsilon^3 \theta_1(s) + 0(\varepsilon^5), \quad x_e(s) = x_0(s) + \varepsilon^2 x_1(s) + 0(\varepsilon^4), \\ y_e(s) &= \varepsilon y_0(s) + \varepsilon^3 y_1(s) + 0(\varepsilon^5), \quad f_e(s) = f_0(s) + \varepsilon^2 f_1(s) + 0(\varepsilon^4), \end{aligned} \quad (\text{A1.15})$$

$$\sin \theta_e = \varepsilon \theta_0 + \frac{1}{6} \varepsilon^3 (-\theta_0^3 + 6\theta_1) + 0(\varepsilon^5), \quad \cos \theta_e = 1 + \frac{1}{2} \varepsilon^2 (-\theta_0^2) + 0(\varepsilon^4), \quad (\text{A1.16})$$

Using the above approximation to Eq. (A1.11) and taking the first two terms in each equation, we can obtain:

$$\frac{dx_0}{ds} = 1, \quad \frac{dx_1}{ds} = -\frac{1}{2} \theta_0^2 \quad (\text{A1.17})$$

$$\frac{dy_0}{ds} = \theta_0, \quad \frac{dx_1}{ds} = \theta_1 - \frac{1}{6}\theta_0^3 \quad (\text{A1.18})$$

$$\frac{d^2\theta_0}{ds^2} = -f_0\theta_0, \quad \frac{d\theta_1}{ds} = s - f_1\theta_0 - f_0\theta_1 + \frac{1}{6}f_0\theta_0^3 \quad (\text{A1.19})$$

The boundary conditions can be re-written as:

$$\begin{aligned} x_0(0) = x_1(0) = 0, \quad y_0(0) = y_1(0) = 0, \\ \theta_0(0) = \theta_1(0) = 0, \quad \theta_0(1) = \theta_1(1) = 0, \end{aligned} \quad (\text{A1.20})$$

Following,<sup>86</sup> we can solve Eq. (A1.19) with the above boundary conditions as

follows:

$$\theta_0 = C \sin(\pi s), \quad \theta_1 = \frac{C^3}{192} \sin(3\pi s) + \frac{s}{\pi^2} (1 + \cos(\pi s)), \quad (\text{A1.21})$$

where constant  $C$  is determined by the external force  $F$ . We can also solve for the normalized force  $f_e$  as:

$$f_0 = \pi^2, \quad f_1 = \frac{\pi^2 C^2}{8} + \frac{2}{\pi C}, \quad f_e = \pi^2 + \varepsilon^2 \left( \frac{\pi^2 C^2}{8} + \frac{2}{\pi C} \right) + 0(\varepsilon^4) \quad (\text{A1.22})$$

From Eqs. (A1.17) and (A1.18) and boundary conditions, we can obtain:

$$x_0 = s, \quad x_1 = \frac{C^2}{4} \left( \frac{1}{2\pi} \sin(2\pi s) - s \right), \quad y_0 = \frac{C}{\pi} (1 - \cos(\pi s)) \quad (\text{A1.23})$$

Thus, the normalized lateral displacement of the moving end of the PVDF film,  $\delta$ , and the maximum height of the PVDF film deflection,  $h_{\max}$ , can be calculated as

$$\delta = 1 - x_e(1) = \frac{1}{4} C^2 \varepsilon^2 + 0(\varepsilon^4), \quad h_{\max} = y(1) = \frac{2}{\pi} C \varepsilon + 0(\varepsilon^3) \quad (\text{A1.24})$$

We can approximately calculate the electric charge given by Eq. (A1.13) using Eqs. (A1.15), (A1.21) and (A1.22) as follows:

$$Q_e = 2d_{31}c_{11} \frac{I}{Lh} \int_0^1 \left\{ \left[ \pi^2 + \varepsilon^2 \left( \frac{\pi^2 C^2}{8} + \frac{2}{\pi C} \right) \right] \left[ 1 + \frac{1}{2} \varepsilon^2 (-C^2 s \sin^2 \pi s) \right] \right\} ds \quad (\text{A1.25})$$

where in the above approximation, we drop the terms that contain  $O(\varepsilon^4)$ . Using the approximation for the film end displacement  $\delta = \frac{1}{4} C^2 \varepsilon^2$  given by Eq. (A1.24), we can simplify Eq. (A1.25) as

$$Q_e = 2d_{31}c_{11} \frac{I}{Lh} \left( \pi^2 + \frac{1}{2} \pi^2 \delta + \frac{\varepsilon^3}{\pi \sqrt{\delta}} \right) (1 - \delta) \quad (\text{A1.26})$$

or

$$Q_e \approx 2d_{31}c_{11} \frac{I}{Lh} \pi^2 \left( 1 + \frac{1}{2} \delta \right) (1 - \delta) \quad (\text{A1.27})$$

Figure A2 shows the simulated relationship between the normalized displacement  $\delta$  and the normalized accumulated charge  $Q_e$  that is generated during the buckling motion.



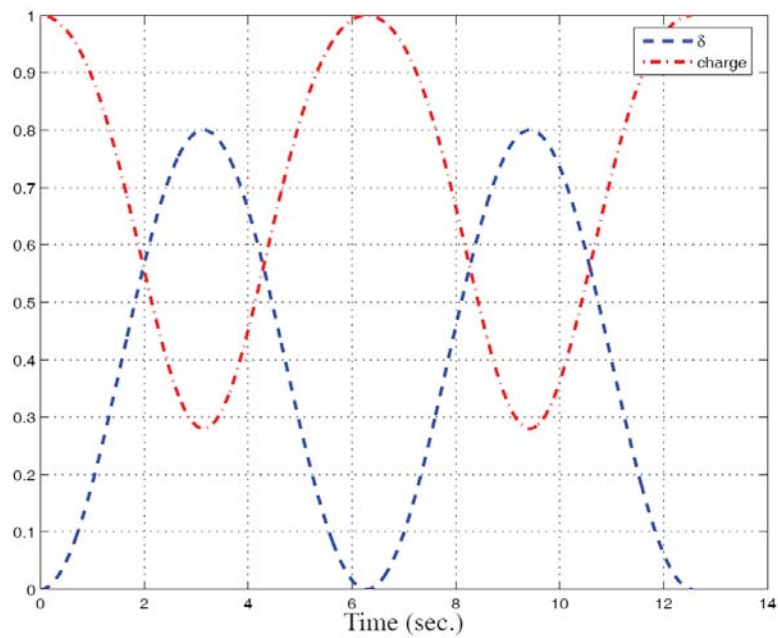


**Figure A2** Simulated relationship between the normalized accumulated charge  $Q_e$  and the normalized end displacement  $\delta$  during a buckling motion.

## APPENDIX B

### LABORATORY EQUIPMENT SETUP

The purpose of this section is to document the laboratory setup settings used during the experiments. This includes wiring diagrams, custom programming routines and software/hardware settings required for the system's correct operation.

#### B.1 Hardware wiring diagrams

Following wiring diagrams describe electrical connections between laboratory equipment elements. Figure B1 below shows the power connections:

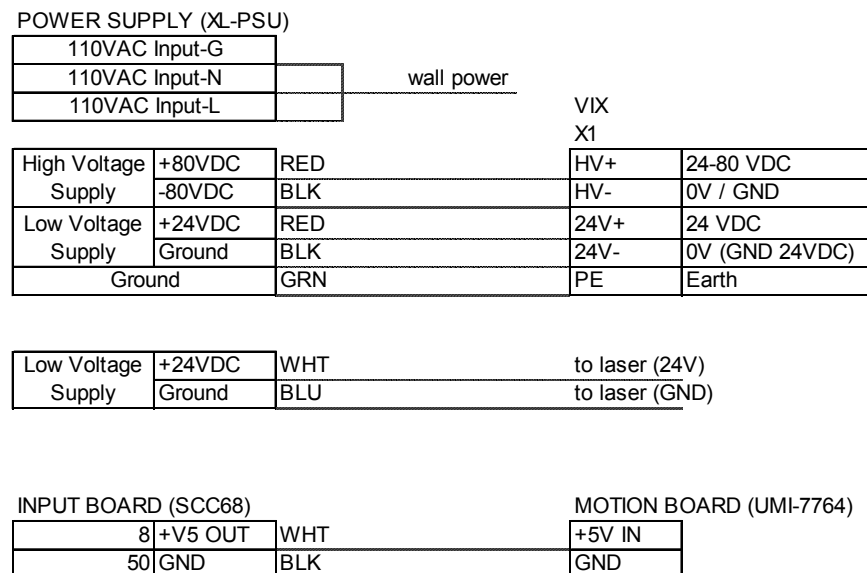


**Figure B1 Power wiring.**

Laser lateral distance gauge wiring is shown in Figure B2:

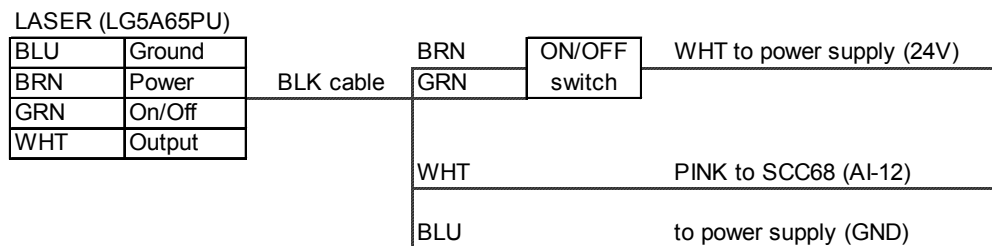


**Figure B2 Laser gauge wiring.**

Figure B3 presents the linear stage electrical connections:

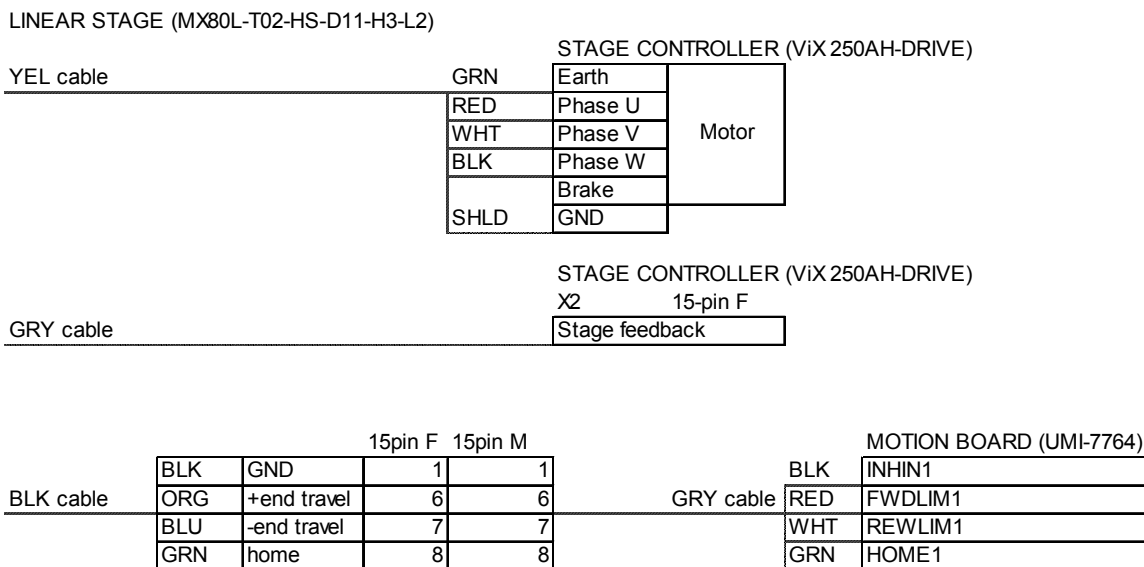


**Figure B3 Linear stage wiring.**

Linear stage controller wiring is shown in Figure B4:

## STAGE CONTROLLER (ViX 250AH-DRIVE)

X1

HV+	24-80 VDC
HV-	0V / GND
24V+	24 VDC
24V-	0V (GND 24VDC)
PE	Earth

to power supply (XL\_PSU)  
(see power wiring)

X2 15-pin F

Stage feedback
----------------

GRY to linear stage

X3 9-pin

Serial connection
-------------------

GRY to computer COM1

X4 15pin M

ANA1+ (input)	1
ANA1- (input)	2
0V	3
/Z index (output)	4
Z index (output)	5
Fault (output)	6
STEP- (input)	7
DIR- (input)	8
A- (output)	9
B- (output)	10
Energize (input)	11
STEP+ (input)	12
DIR+ (input)	13
A+ (output)	14
A- (output)	15

15-pin F

1-ORG
2-GRN
3-REDBLK
4-BLK
5-WHTBLK
6-BLU
14-WHT
15-RED

MOTION BOARD (UMI-7764)

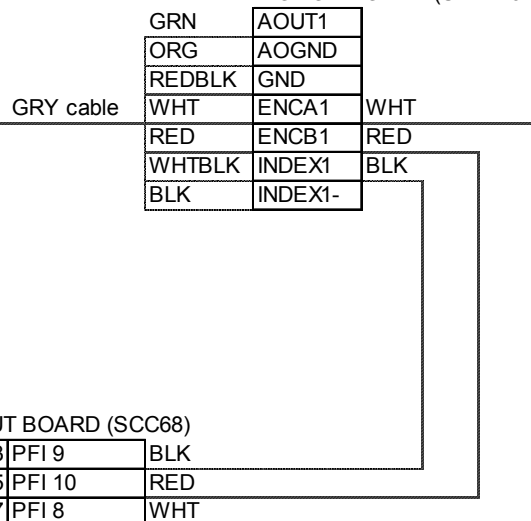
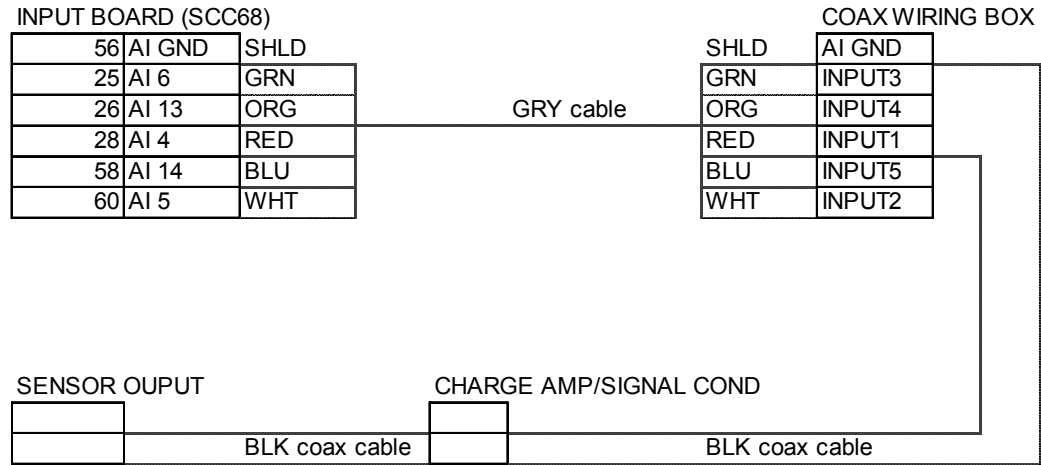


Figure B4 Linear stage controller wiring.

Figure B5 shows the connections for the piezoelectric sensor output:



**Figure B5 Sensor signal wiring.**

This completes the electrical connection setup for the laboratory setup.

## B.2 Software settings

This sections presents software settings and custom programs used in the system setup.

### B.2.1 Stage controller settings

Following are settings for the stage controller (ViX 250AH-DRIVE) operation and communication with the computer. Connection details are shown in Figure B6:

ViX A H servo configuration - 4407SUP.CFG

Axis Motor Tuning I/O Other

Address  Click 'Upload' to retrieve current settings for this axis.

Serial number

Product description  Click 'Download' to update the axis with your changes.

Product software type

Software revision

Upload Download Open Save Print Done Help

Figure B6 ViX settings – address setup.

Motor control settings are shown in Figure B7:

ViX A H servo configuration - (untitled)

Axis Motor Tuning I/O Other

Cont. stall current	0.8	Amps-RMS
Pole Pitch	13.0	mm
Resolution	5.0	microns (post quad)
Rated speed	3.00	m/s
Feedback type	encoder	
Unloaded inertia (mass)	0.2	Kg
Static brake	not fitted	
Alternate commutation	not selected	
Thermal protection	sensor fitted	
Invert hall	No	
Force constant (Kf)	4.100	N/A peak
Viscous damping	0.5	N/m/sec
Resistance (line - line)	9.50	Ohms
Inductance (line - line)	3.60	mH
Thermal time constant	80	seconds
Motor I.D. 4	Motor type (MT) 49412	

Operating mode (M command)

Velocity amplifier (default)

Torque amplifier

Position control

Direction sense (H command)

CW - positive signal

CCW - positive signal

Tracking limit (TL)

Peak current ratio (PC)

Drive current clamp (CL)

Note that changing the motor or mode updates certain system variables in these setup pages e.g. PIVF gains, Index Position (IX), etc...

Upload Download Open Save Print Done Help

Figure B7 ViX settings – motor setup.

Figure B8 presents motion tuning settings:

The screenshot shows a software window titled "ViX A H servo configuration - 4407SUP.CFG". The window has five tabs: "Axis", "Motor", "Tuning", "I/O", and "Other". The "Tuning" tab is selected and active. It contains five rows of settings, each with a label and a numerical input field with up/down arrows:

Parameter	Value
Feedforward (GF)	20.00
Integral (GI)	0.00
Proportional (GP)	0.00
Velocity (GV)	100.00
Filter time (FT)	0

At the bottom of the window, there is a row of seven buttons: "Upload", "Download", "Open", "Save", "Print", "Done", and "Help".

**Figure B8 ViX settings – tuning parameters.**

Input and output configurations are shown in Figure B9:

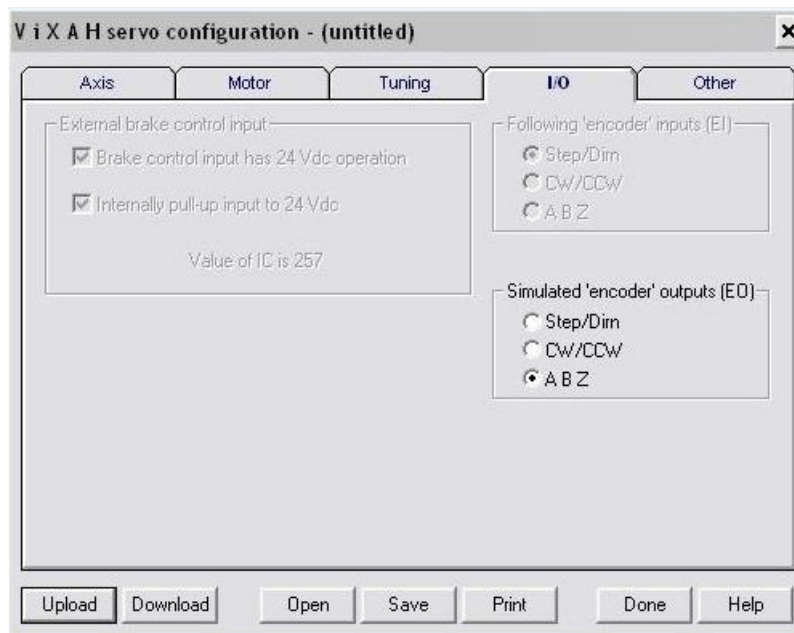


**Figure B9 ViX settings – input/output setup.**



All other settings are presented in Figure B10:

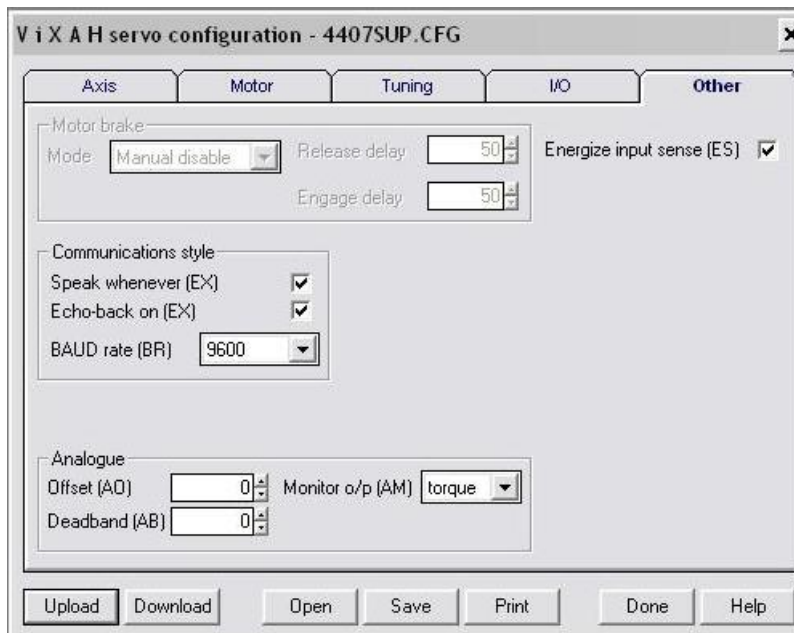
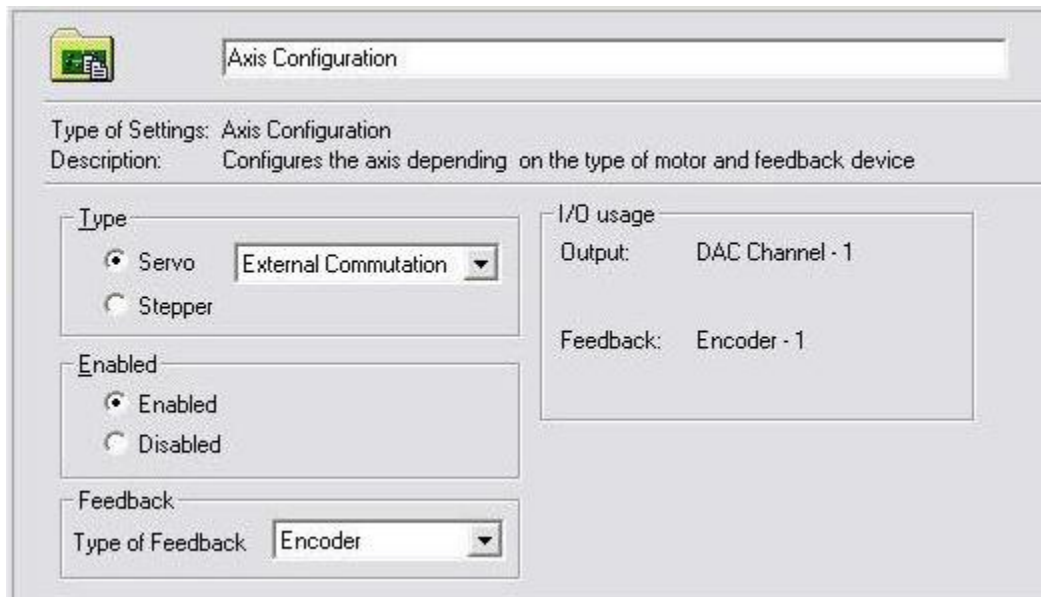


**Figure B10 ViX settings – other parameters.**

This completes the linear stage controller settings necessary for correct operation and communication with the computer.

### *B.2.2 National Instruments Motion Assistant Explorer settings*

The Motion Assistant Explorer (MAX) program ensures proper communication between National Instruments software and the linear stage. Its key settings include the axis configuration shown in Figure B11:



**Axis Configuration**

Type of Settings: Axis Configuration  
Description: Configures the axis depending on the type of motor and feedback device

**Type**

Servo  Stepper

External Commutation

**Enabled**

Enabled  Disabled

**Feedback**

Type of Feedback: Encoder

**I/O usage**

Output: DAC Channel - 1

Feedback: Encoder - 1

**Figure B11 Motion Assistant Explorer settings – axis configuration.**

Additional setup includes motion input and output settings shown in Figure B12:

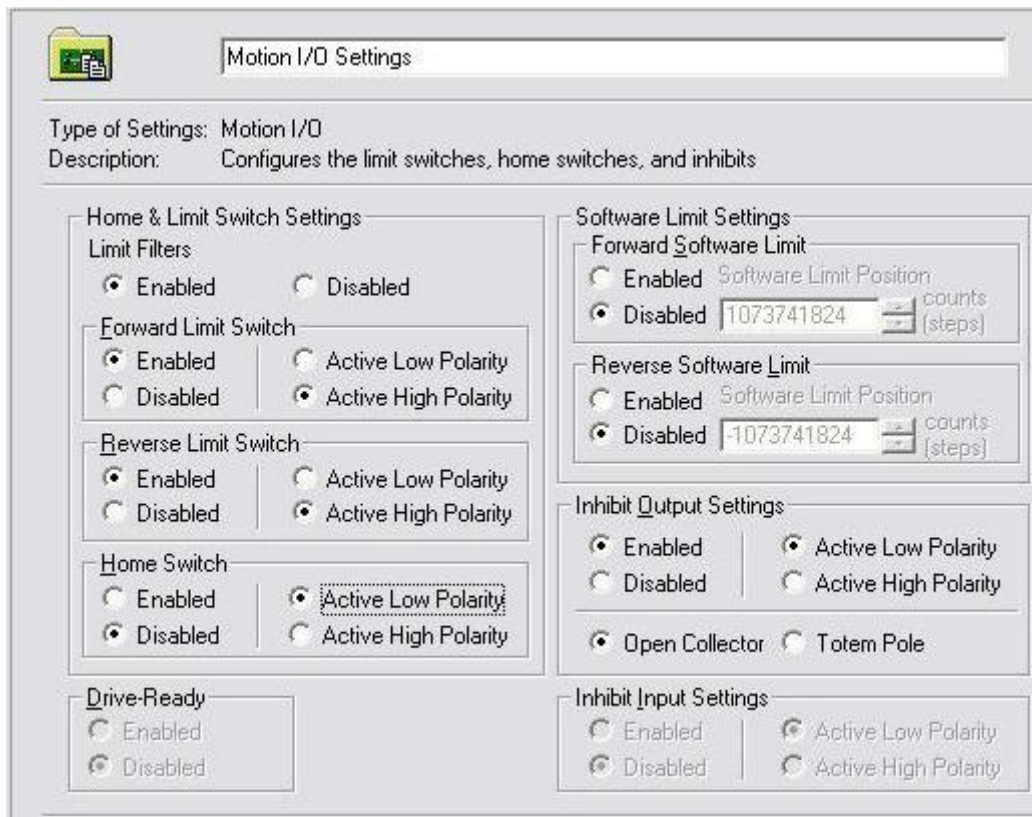


**Figure B12 Motion Assistant Explorer settings – motion limits setup.**

With the Motion Assistant Explorer characteristics set up correctly, additional software such as LabVIEW, discussed in the next section, may be used to control the linear stage.

### *B.2.3 LabVIEW controls and custom diagrams*

Custom written LabVIEW software is used to control linear stage movements, gather and display data and save information to file. Figure B13 shows the user display view of this setup:

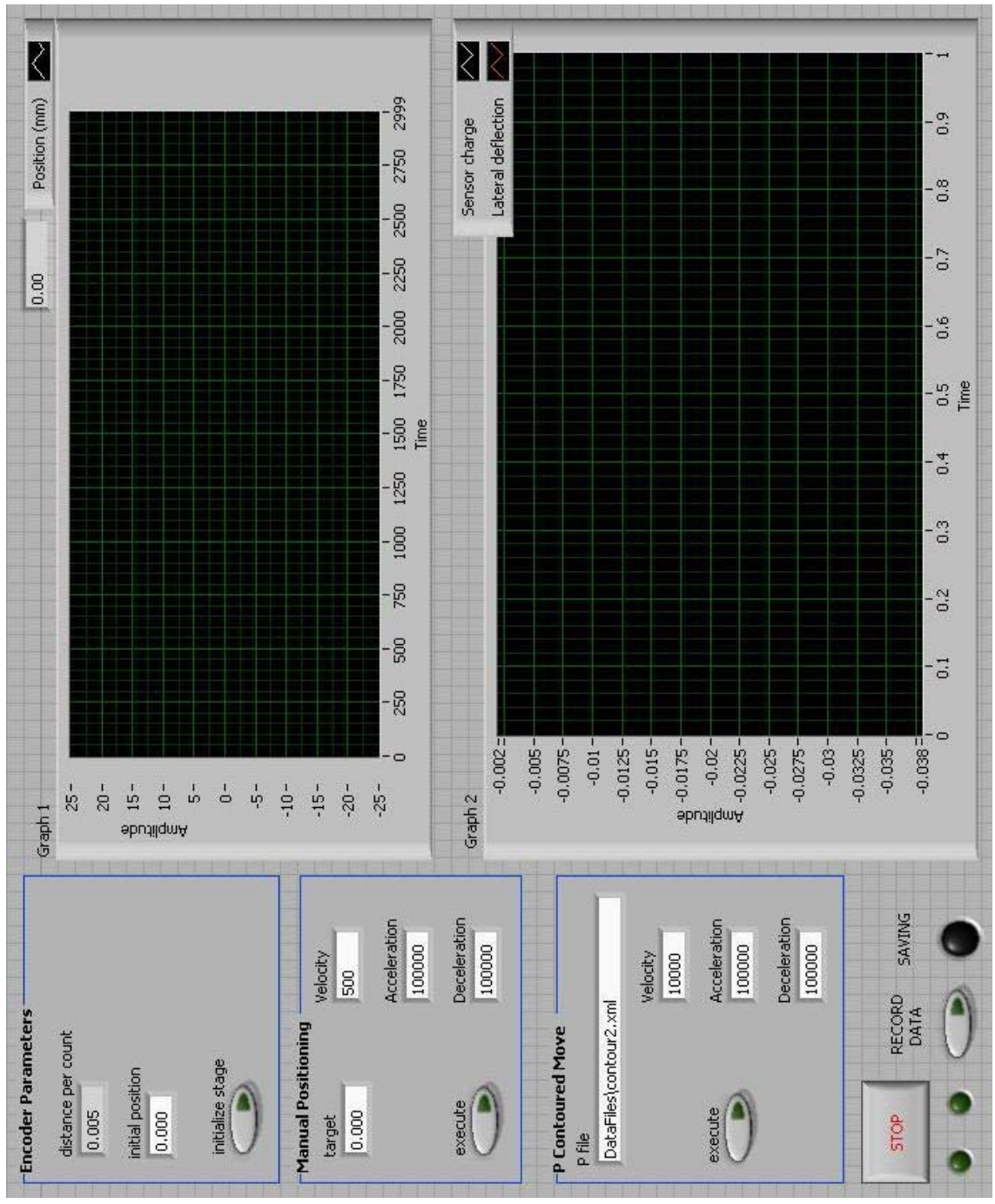


Figure B13 LabVIEW routine – operator view.

Custom LabVIEW routines shown in Figure B14 are responsible for gathering and saving data:

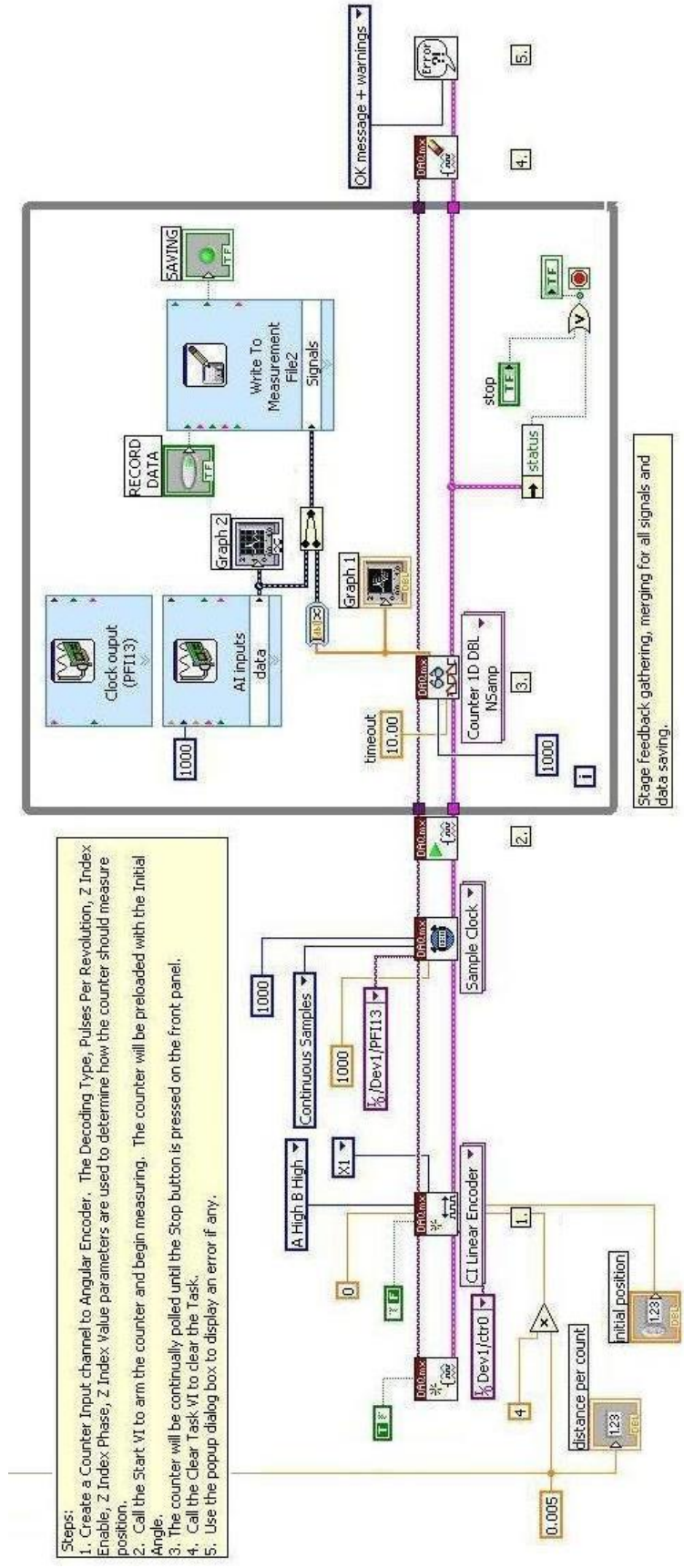


Figure B14 LabVIEW routine – initialization, data acquisition and file transfer.

The elements shown in Figure B15 allow for execution of the linear stage movements:

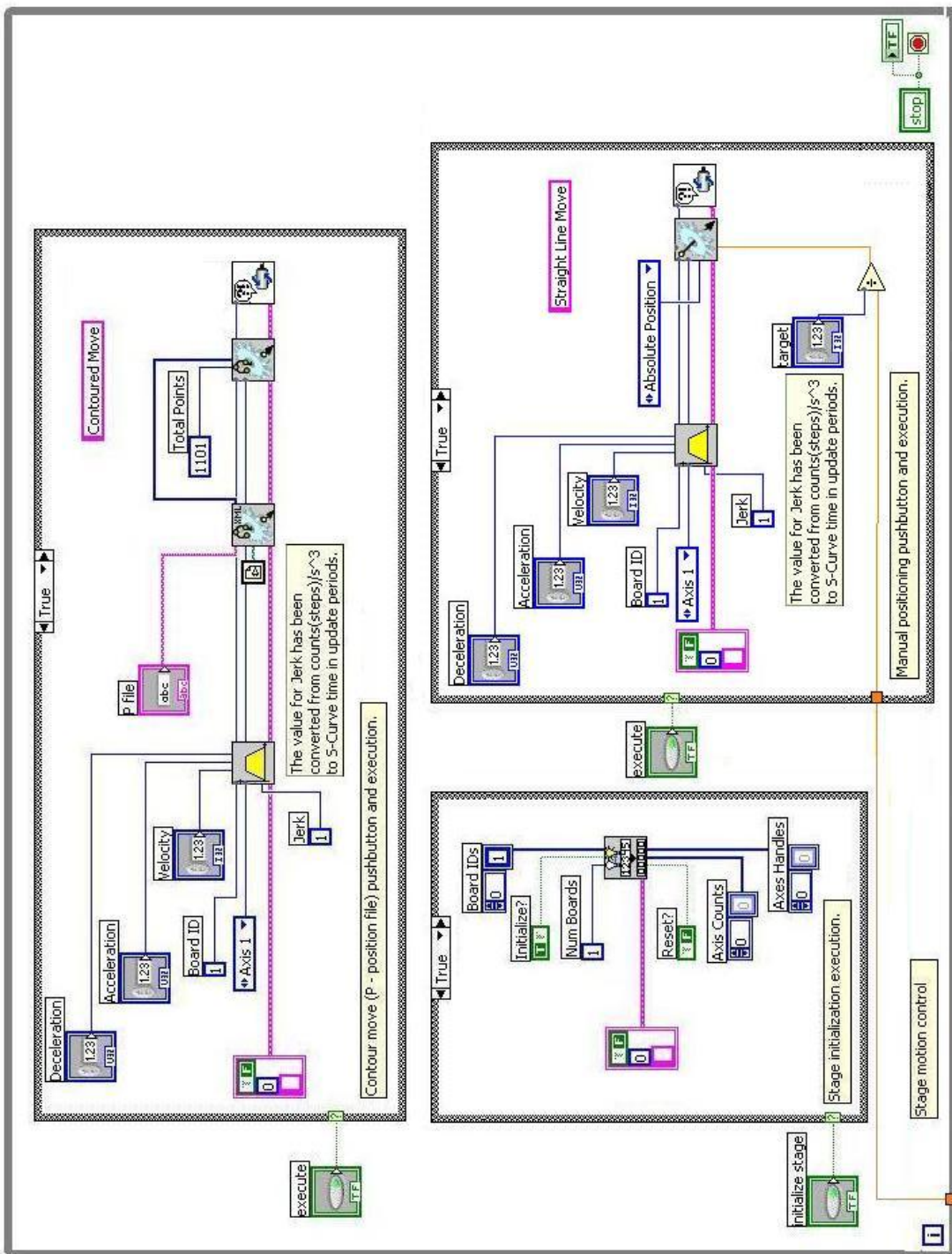


Figure B15 LabVIEW routine – linear stage path execution.



Additional LabVIEW settings used are described in the following section.

#### B.2.4 LabVIEW settings

Following are LabVIEW input and output settings used within the routine presented earlier. Figure B16 shows the internal clock setup used for timing of the feedback signals:

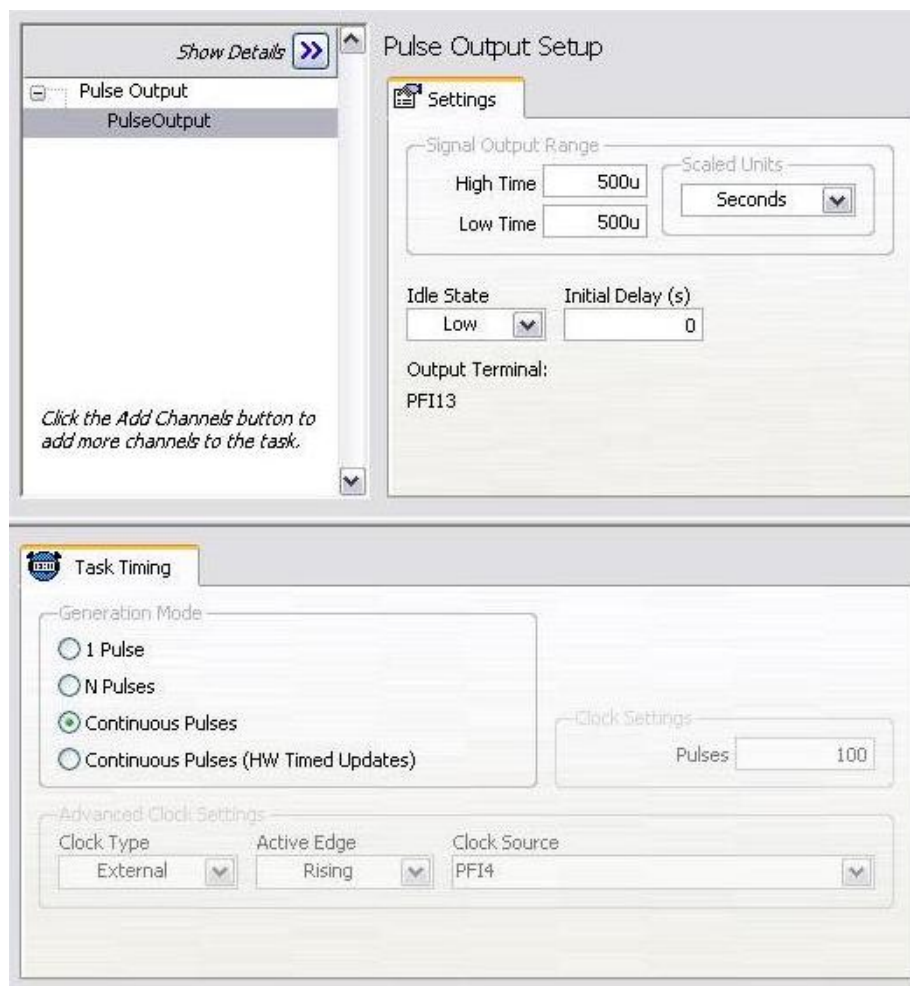
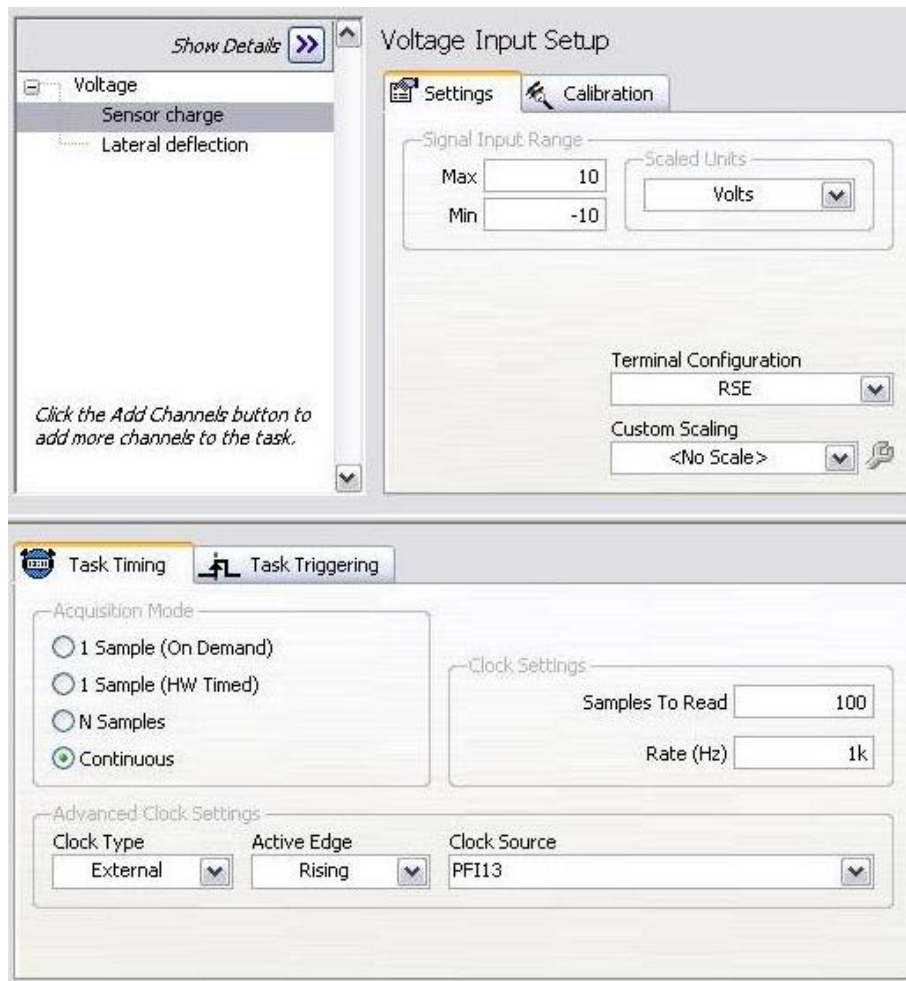


Figure B16 LabVIEW settings – internal clock setup.

Figure B17 shows the signal input settings:



**Figure B17 LabVIEW settings – input setup.**

This completes the description of the LabVIEW system control settings.

### *B.2.5 Microsoft Excel templates*

Linear stage motion paths were defined using a simple Microsoft Excel template shown in Figure B18:

	counts	mm		0	0
				10	-2.368
amplitude =	1200	6		20	-9.462
				30	-21.26
				40	-37.7
frequency =	1	hz		50	-58.73
step =	10			60	-84.27
length =	5			70	-114.2
				80	-148.4
total travel	12	mm		90	-186.8
				100	-229.2
				110	-275.4
				120	-325.2
				130	-378.5
				140	-435.1
				150	-494.7
				160	-557
				170	-621.9
				180	-689.1
				190	-758.3
				200	-829.2

**Figure B18 Excel path definition settings**

This allows for defining the motion characteristics (using values on the left) and creating a position value vector (shown on the right). Visual path verification is also available using a graph as shown in Figure B19:

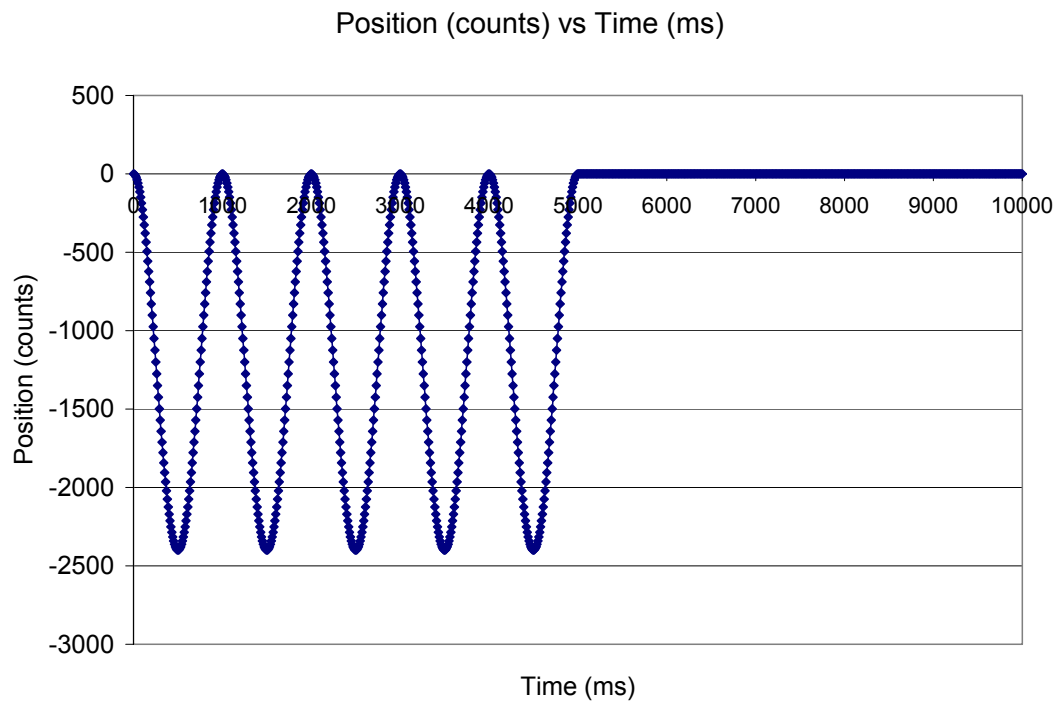


**Figure B19 Path output graph**

As discussed earlier in section III.4.1, the data can be then converted into a format readable by the LabVIEW software for execution of the linear stage motion.

**VITA**

Name:

Bartosz Mika

Address:

c/o: Dr. Hong Liang

Texas A&M University

Department of Mechanical Engineering

TAMU 3123

College Station, TX 77843

Email Address:

bzmika@tamu.edu

Education:

B.S., Mechanical Engineering, University of Washington, 2002

M.S. Mechanical Engineering, Texas A&M University, 2007